

1 **A Model-Driven Meta-Analysis Supports the Emerging Consensus** 2 **View that Inhibitory Neurons Dominate BOLD-fMRI Responses**

3 Nicolas Sundqvist^{†,1}, Henrik Podéus^{†,1}, Sebastian Sten², Maria Engström^{3,4}, Salvador Dura-Bernal^{5,6}
4 Gunnar Cedersund^{1,4,7,*}

5 ¹Department of Biomedical Engineering, Linköping University, Linköping, Sweden

6 ²Drug Metabolism and Pharmacokinetics, Research and Early Development, Cardiovascular, Renal and
7 Metabolism (CVRM), BioPharmaceuticals R&D, AstraZeneca, Gothenburg, Sweden

8 ³Department of Health, Medicine and Caring Sciences, Linköping University, Linköping, Sweden

9 ⁴Center for Medical Image Science and Visualization (CMIV), Linköping University, Linköping, Sweden

10 ⁵Department of Physiology and Pharmacology, State University of New York (SUNY) Downstate Health Sciences
11 University, Brooklyn, NY, USA

12 ⁶Center for Biomedical Imaging and Neuromodulation, Nathan Kline Institute for Psychiatric Research,
13 Orangeburg, NY, USA

14 ⁷School of Medical Sciences and Inflammatory Response and Infection Susceptibility Centre (iRISC), Faculty of
15 Medicine and Health, Örebro University, Örebro, Sweden

16

17 † Authors contributed equally.

18 * Corresponding author: Gunnar Cedersund, Email: gunnar.cedersund@liu.se

19

20 Address: Department of Biomedical Engineering, Linköping University, 58185 Linköping, Sweden. Phone: +4613-
21 28 67 26

22

23 Abstract

24 Functional magnetic resonance imaging (fMRI) is a pivotal tool for mapping neuronal activity in the
25 brain. Traditionally, the observed hemodynamic changes are assumed to reflect the activity of the most
26 common neuronal type: excitatory neurons. In contrast, recent experiments, using optogenetic
27 techniques, suggest that the fMRI-signal instead reflects the activity of inhibitory interneurons.
28 However, these data paint a complex picture, with numerous regulatory interactions, and where the
29 different experiments display many qualitative differences. It is therefore not trivial how to quantify
30 the relative contributions of the different cell types and to combine all observations into a unified
31 theory. To address this, we present a new model-driven meta-analysis, which provides a unified and
32 quantitative explanation for all data. This model-driven analysis allows for quantification of the relative
33 contribution of different cell types: the contribution to the BOLD-signal from the excitatory cells is <20
34 % and 50-80 % comes from the interneurons. Our analysis also provides a mechanistic explanation for
35 the observed experiment-to-experiment differences, e.g. a biphasic vascular response dependent on
36 different stimulation intensities and an emerging secondary post-stimulation peak during longer
37 stimulations. In summary, our study provides a new, emerging consensus-view supporting the larger
38 role of interneurons in fMRI.

39 Abbreviations

40 AUC – area under the curve

41 BOLD – blood oxygen level-dependent

42 CBF – cerebral blood flow

43 CI – confidence interval

44 CMRO₂ – cerebral metabolic rate of oxygen

45 fMRI – functional magnetic resonance imaging

46 GABA – γ -aminobutyric acid

47 Hb – haemoglobin

48 HbO – oxygenated haemoglobin

49 HbR – deoxygenated haemoglobin

50 HbT – total haemoglobin

51 HRF – hemodynamic response function

52 LDF – laser doppler flowmetry

53 NO – nitric oxide

54 NOS – nitric oxide synthase

55 NPY – neuropeptide Y

56 NVC – neurovascular coupling

57 OIS – optical intrinsic signal

58 PGE₂ – Prostaglandin E₂

59 SOM – somatostatin

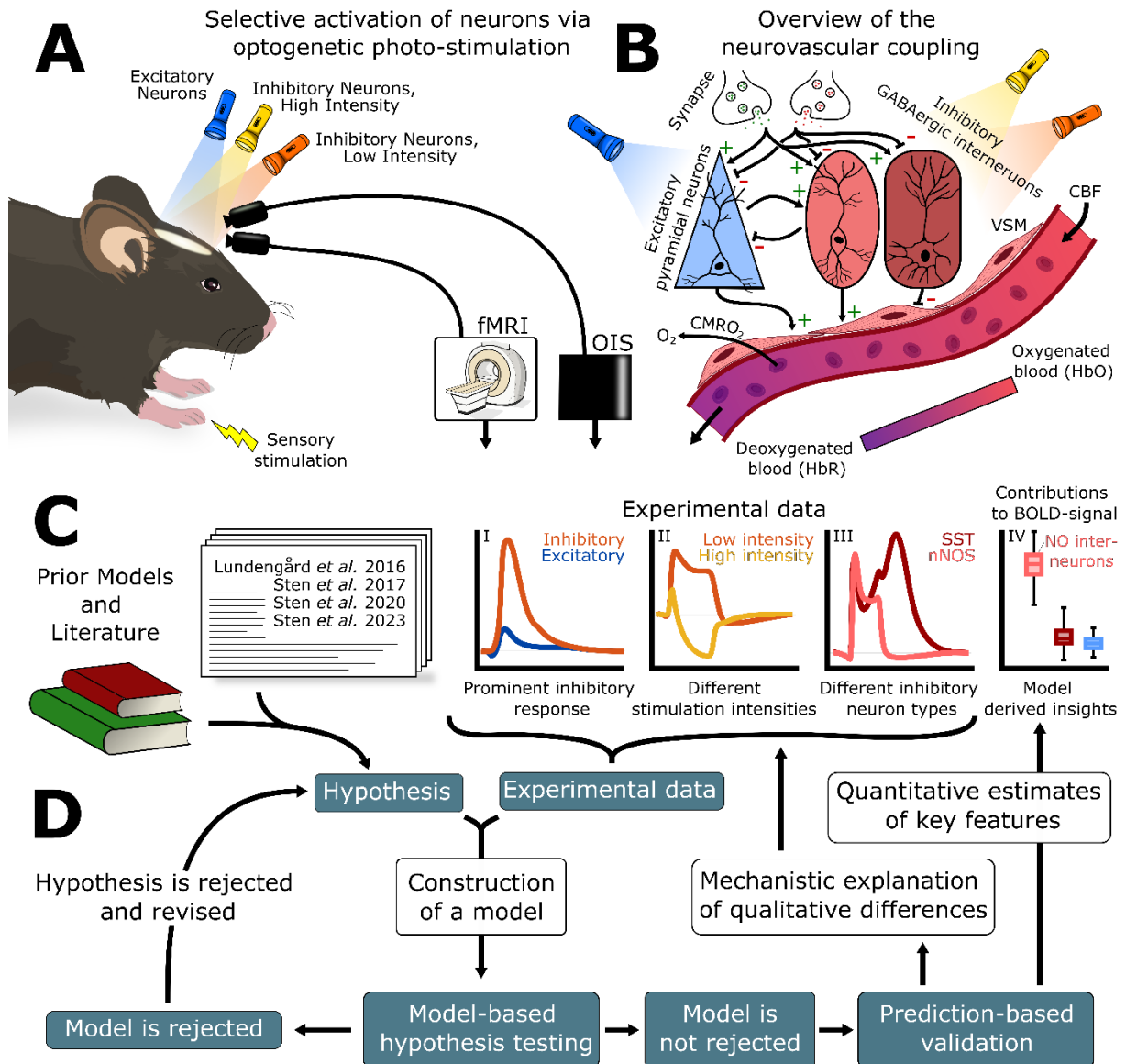
60 VGAT – vesicular GABA transport

61

62 Keywords: fMRI, BOLD, OIS, NVC, mathematical modelling, inhibitory neurons.

63 Introduction

64 Functional magnetic resonance imaging (fMRI) is a cornerstone of neuroimaging, as it allows
65 researchers and clinicians to assess neuronal activation in response to stimuli (Figure 1A)(Gore, 2003;
66 Kim and Ogawa, 2012). fMRI does not measure neuronal activity directly but is instead sensitive to
67 changes in the ratio of oxygenated and deoxygenated blood (Ogawa *et al.*, 1990; Kim and Ogawa,
68 2012). Thus, the neuronal activity determined from fMRI reflects temporal changes in the blood
69 oxygenation levels i.e., the so-called Blood Oxygen Level-Dependent (BOLD) response (Ogawa *et al.*,
70 1990; Hillman, 2014). This fMRI-BOLD response relies on a balance between the cerebral metabolic
71 rate of oxygen (CMRO₂) and the active regulation of the cerebral blood flow (CBF), both of which are
72 coupled to the neuronal activity via the neurovascular coupling (NVC)(Figure 1B)(Logothetis, 2003;
73 Hillman, 2014). The conventional interpretation of the fMRI-BOLD signal generally assumes that
74 changes in the BOLD signal echo increases and decreases in excitatory, i.e. stimulating, neuronal activity
75 (Logothetis *et al.*, 2001; Logothetis, 2008). In other words, the general assumption is that regions with
76 excitatory activation upregulate the CBF, which leads to an increased fMRI-BOLD signal. In the same
77 way, the assumption has been that activation of inhibitory neurons should inhibit further activity in
78 nearby neurons, leading to a decrease in the fMRI-BOLD signal.



79

80

81 **Figure 1: An overview of the study. A)** Highly detailed data has been collected from mice, using optogenetic

82 stimulation of inhibitory (orange and yellow) and excitatory (blue) neurons, as well as sensory stimulation. These

83 data measure the changes in the blood oxygen saturation, either using fMRI-BOLD or optical intrinsic signalling

84 (OIS) imaging. **B)** Overview of the neurovascular coupling (NVC). Neurotransmitters are released from the synaptic

85 cleft, which either upregulate or downregulate surrounding neurons. Excitatory pyramidal neurons excite

86 surrounding neurons and inhibitory GABAergic interneurons inhibit surrounding neuronal activity. The process of

87 releasing neurotransmitters is energy-intensive, and the cerebral metabolic rate of oxygen (CMRO₂) is high. To

88 replenish metabolites, some neurons can dynamically control the dilation and constriction of cerebral blood

89 vessels through the release of vasoactive substances that act on the vascular smooth muscles (VSM) surrounding

90 the blood vessel. **C)** These highly detailed data show: I) differences between inhibitory and excitatory stimulations

91 (orange vs blue), II) stimulation intensity dependencies between low-intensity (orange line) and high-intensity

92 (yellow line), and III) different response profiles when inhibitory stimulation is applied to the different GABAergic

93 interneurons (light red-NO and crimson-SST). **D)** These different attributes in data can be analysed using

94 mathematical modelling. A hypothesis is formulated as a model and evaluated towards the experimental data.

95 The hypothesis is rejected if it cannot describe the data, which leads to revision of the hypothesis. This is repeated

96 until a hypothesis that cannot be rejected is obtained. Using this unrejected model, prediction-based model

97 validation is obtained when the model can predict data it has not been trained to. Finally, such a validated model

is used to obtain mechanistic explanations of qualitative differences (I-III) and to estimate and quantify key

98 *features (IV). Herein, this approach is used to show that NO-interneurons (IV) are the biggest contributors to the*
99 *BOLD response.*

100 Contrary to this traditional interpretation, several recent studies (Vazquez *et al.*, 2014; Uhlirova *et al.*,
101 2016; Vazquez, Fukuda and Kim, 2018; Desjardins *et al.*, 2019; Echagarruga *et al.*, 2020; Krawchuk *et*
102 *al.*, 2020; Lee *et al.*, 2020; Moon *et al.*, 2021) show that γ -aminobutyric acid (GABA)ergic inhibitory
103 interneuron populations affect the regulation of CBF and blood oxygen saturation to a larger extent
104 than excitatory neurons (Figure 1C, I). These studies typically use optogenetics, i.e. genetically modified
105 mice to with a light pulse selectively activate either excitatory or inhibitory neurons (Figure 1A).
106 Following the stimulation, hemodynamic responses, such as CBF and BOLD-signal responses, are
107 measured using e.g. fMRI or optical imaging of the optical intrinsic signal (OIS). These measurements
108 generally imply that the relationship between the BOLD response and neuronal activity is more
109 complicated than conventionally assumed. This is in part due to the high complexity of the involved
110 regulatory systems, which makes it hard to quantify the contribution of the different cell types to the
111 NVC. Furthermore, the differences in the experimental conditions of these studies mean that their
112 findings display numerous qualitative and quantitative differences in the observed responses (e.g.
113 Figure 1C, I-III). In summary, as the mechanisms behind these qualitative differences are not fully
114 understood, obtaining a unified explanation for all these responses is challenging (Figure 1C, IV).

115 An approach to establishing such a unified explanation is mathematical modelling. Mathematical
116 modelling allows for integration of prior understanding with newer experimental findings and
117 hypotheses, to gain a more holistic representation of our mechanistic understanding of the NVC (Figure
118 1D). There have been previous model efforts that have investigated NVC mechanisms (Griffeth and
119 Buxton, 2011; Havlicek *et al.*, 2015; Kim and Ress, 2016; Lundengård *et al.*, 2016; Di Volo *et al.*, 2019;
120 Sten *et al.*, 2020, 2023; Moon *et al.*, 2021; Tesler, Linne and Destexhe, 2023). However, no existing
121 model can provide a mechanistic explanation for the new optogenetics data (Vazquez, Fukuda and Kim,
122 2018; Lee *et al.*, 2020; Moon *et al.*, 2021), that indicates a larger role for interneurons.

123 In this work, we present a mathematical framework that: i) quantifies cell-type-specific contributions
124 to the fMRI-BOLD signal and ii) can explain the qualitative differences in the vasoactive response across
125 multiple experiments. By aggregating and simultaneously analysing data from multiple studies, this
126 framework allows us to establish a model-driven meta-analysis of the mechanisms making up the NVC.
127 This approach presents a critical step towards forming a consensus view of how inhibitory neurons
128 contribute to the NVC, a view which contradicts the traditional interpretation of the fMRI-BOLD signal.
129 As such, the qualitative and quantitative explanations presented in this work argue in support of a
130 paradigm shift in how neuroimaging can, and cannot, be used to infer neuronal activity.

131

132 Results

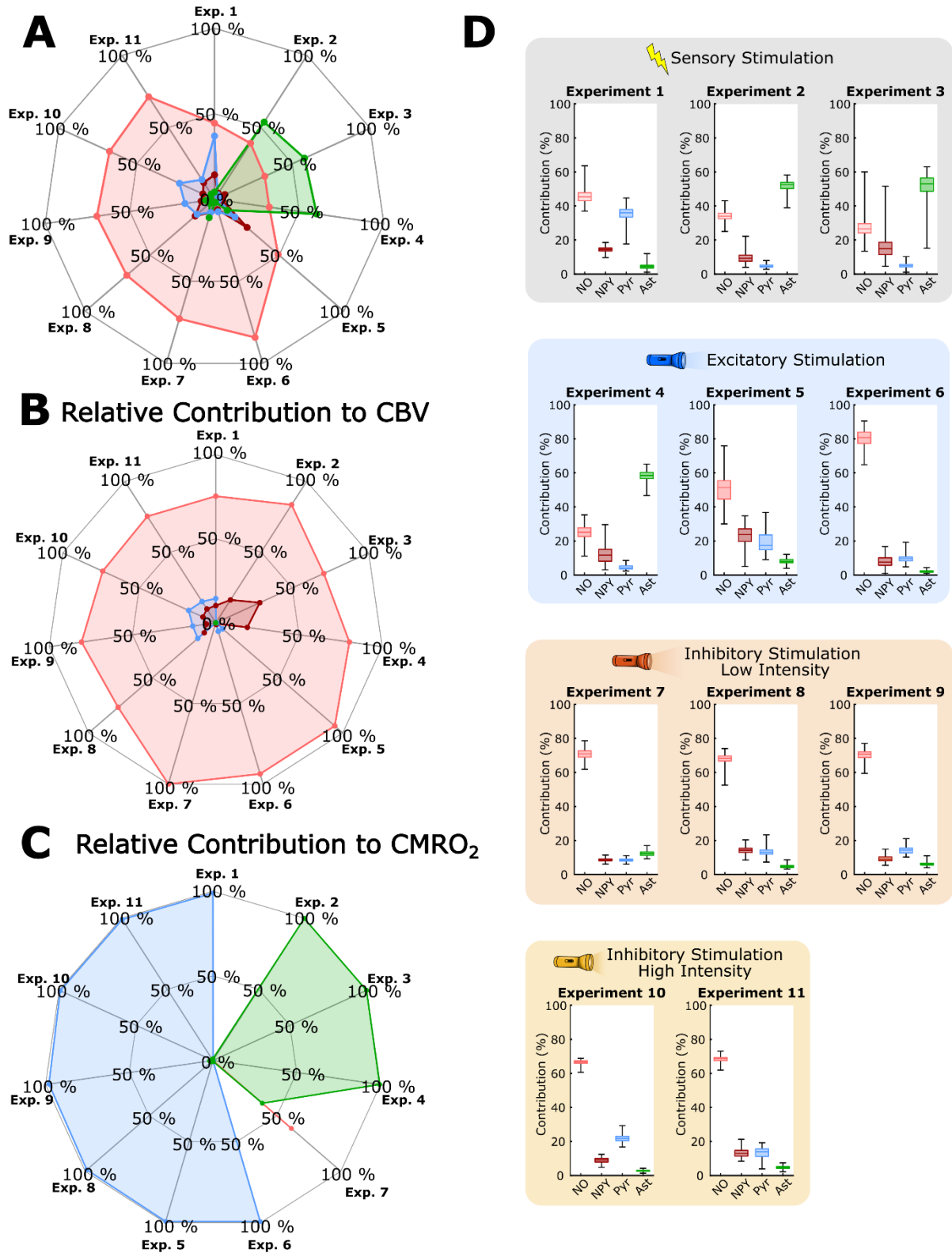
133 We here present a mechanistic, model-driven, meta-analysis that supports the emerging consensus-
134 view that inhibitory neurons dominate the vascular regulation of the NVC. Our analysis offers: i)
135 quantitative estimates of the cell-type-specific contributions to the neurovascular response (Figure 2)
136 and ii) mechanistic explanations of the qualitative differences between observed responses across
137 different studies (Figures 3-7). More specifically, the quantitative estimations of the cell-type-specific
138 contribution to the BOLD signal are based on a mechanistic model trained on data from 11 different
139 experiments (Figures 2A and D). These results show that the inhibitory neurons contribute >50 % of
140 the BOLD signal in 8 of the 11 experiments and >75 % of the vascular response in all experiments (Figure
141 2B).

142 Quantitative cell type contributions to the BOLD signal

143 Our model-based meta-analysis consists of two steps: i) Develop a model that can simultaneously fit
144 data from all considered studies (Figures 1D, 3, 5, and 7) and correctly predict new validation data
145 (Figures 3G-H, and 4), ii) Analyse the validated model, to draw mechanistic conclusions (Figures 3, 6,
146 and S3). Using this model-driven approach to the data analysis, we can quantitatively estimate the
147 contribution of different neuronal populations to the BOLD-response. Compiling these estimates across
148 the 11 different considered experiments, it is clear that inhibitory interneurons contribute more to the
149 BOLD-response than excitatory neurons (Figure 2A and D). Figure 2A illustrates this compilation in the
150 form of a spider plot, where the different neurons (and astrocytes) are represented by colour and their
151 relative contributions to the BOLD-responses for each experiment are plotted along the axes. The 11
152 experiments can be divided into 4 different stimulation paradigms: sensory stimulation, optogenetic
153 stimulation of excitatory neurons, low-intensity optogenetic stimulation of inhibitory neurons, and
154 high-intensity optogenetic stimulation of inhibitory neurons. As can be seen, the combined
155 contributions of the interneurons to the BOLD-signal are around 50-80 %, while the pyramidal neurons
156 contribute <20 %. A more detailed breakdown of the contributions reveals that the combined
157 contributions of NO and neuropeptide Y (NPY) interneurons (Figure 2D, light red and crimson bars) are
158 larger than the contributions of pyramidal neurons (Figure 2D, blue bars) in all 11 experiments. Note
159 that these results cannot be obtained by a mere inspection of the original data and that it stands in
160 contrast to the conventional interpretation of BOLD-fMRI, which assumes that the signal comes
161 predominantly from excitatory pyramidal cells.

Relative Contribution to BOLD Signal

NO Interneurons NPY Interneurons Pyramidal Neurons Astrocytes



162
163
164
165
166

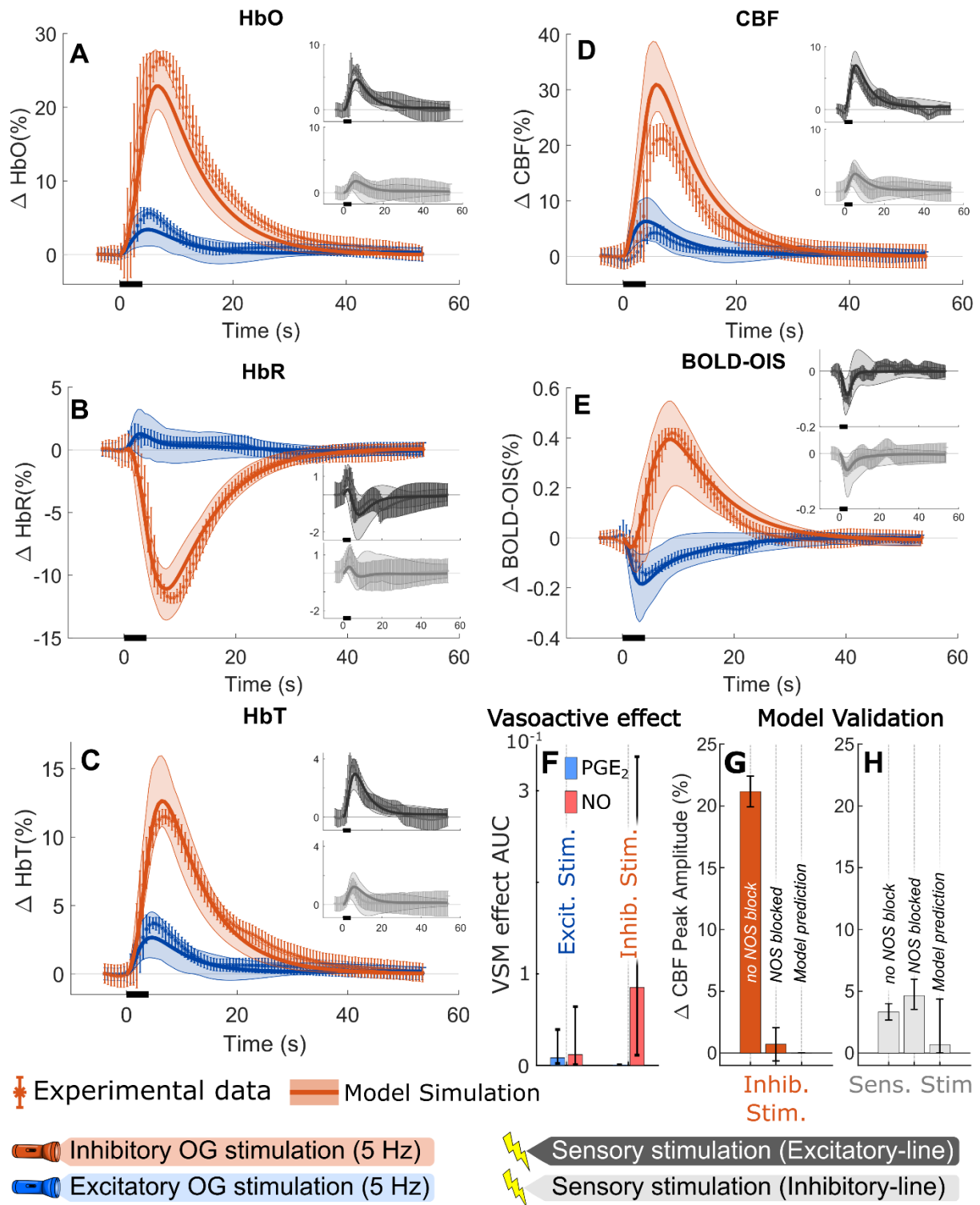
Figure 2: The contribution of different neuronal populations to the BOLD signal, available thanks to our model-based analysis. A) The contribution of four different neural populations: nitric oxide (NO) interneurons (light red), neuropeptide Y (NPY) interneurons (crimson), pyramidal neurons (Pyr, blue), and astrocytes (Ast, green), to the blood oxygen level-dependent (BOLD) signal are presented for 11 different experiments. B) The contributions of

167 *the four neurons (NO, NPY, Pyr, and Ast) to cerebral blood volume (CBV) response in the 11 experiments. C) The*
168 *contributions of the four neurons (NO, NPY, Pyr, and Ast) to cerebral metabolic rate of oxygen (CMRO₂) response*
169 *in the 11 experiments. D) Boxplots detailing the contribution of the four neuronal populations (NO light red, NPY*
170 *crimson, Pyr blue, Ast green), with a 95 % confidence interval, for the 11 experiments presented in A. The*
171 *background of each experiment indicates the type of stimulation that generated these behaviours: grey is a*
172 *sensory stimulation, blue is an optogenetic excitatory stimulation, orange is an optogenetic inhibitory low-*
173 *intensity stimulation, and yellow is an optogenetic inhibitory high-intensity stimulation.*

174 These results show that in 8 out of the 11 cases, the NO-interneurons are the largest contributors to
175 the BOLD-signal, even in the cases of optogenetic excitatory stimulation (Figure 2D, blue box). For the
176 three remaining cases, NO-interneurons still have a large contribution, but the model also attributes a
177 major portion of the BOLD-signal to the astrocytes (Figure 2D, green bars). Consulting the model, we
178 can further investigate this behaviour, by subdividing the quantitative contributions to the BOLD-
179 response into a vascular contribution (changes in CBV, Figure 2B) and a metabolic contribution (changes
180 in CMRO₂, Figure 2C). Studying these sub-contributions, two results stand out: i) NO-interneurons are
181 in all 11 cases the largest contributor to changes in CBV (Figures 2B and S1), and ii) pyramidal neurons
182 are in 7 of 11 cases the largest contributor to changes in CMRO₂ (Figures 2C and S1). Lastly, for the
183 three cases where the astrocytes contributed the most to the BOLD-response (Figure 2A, green), the
184 model attributes this behaviour to the astrocytes having a large effect on the changes in CMRO₂ (Figures
185 2C and S1, green) combined with relatively small changes in the total CBV response. A detailed
186 breakdown of how these quantitative estimates were acquired can be found in Supplementary Material
187 (Supplementary Material section 4). Let us now turn to the second usage of the validated model:
188 providing a mechanistic underpinning for observations, such as the high role of inhibitory neurons.

189 [Inhibitory neurons as a driving force for vascular regulation](#)

190 The results presented above (Figure 2), are contingent on the model being an accurate explanation of
191 the experimental data. The agreement between model and data are shown in Figures 3 and 5. Let us
192 first consider the results in Figure 3, which focuses on the differences between inhibitory and excitatory
193 stimulations (Vazquez, Fukuda and Kim, 2018). This data shows: the measured changes in haemoglobin
194 (oxygenated haemoglobin, HbO, Figure 3A; reduced haemoglobin, HbR, Figure 3B; total haemoglobin,
195 HbT, Figure 3C), the laser Doppler flowmetry (LDF) measurements of CBF (Figure 3D), and the relative
196 percentage change in OIS measurements for BOLD and Hb (Figure 3E). All these data show the result
197 of both an optogenetic excitatory stimulation (blue), and an optogenetic inhibitory stimulation
198 (orange). Note that the data show a larger response in Hb levels, CBF, and OIS-BOLD for stimulation of
199 the inhibitory neurons (Figure 3 orange). Note also that the model simulations (continuous lines and
200 shaded areas) agree with all the main features seen in the data (error bars). For example, changes in
201 HbT following an inhibitory stimulation (Figure 3C, orange) show a prominent peak culminating at
202 around 12 %, at ca 10 sec, for both model simulation and data. Following this peak, the response then
203 subsides and returns to baseline. This qualitative assessment was also confirmed using a χ^2 -test
204 (Equation 11; with a test statistic $f(\theta_{H1}) = 2033.43$ that is lower than the cut-off threshold
205 $\chi^2(\alpha = 0.05, Dof = 3347) = 3482.70$).



206

207

208

209

210

211

212

213

214

215

Figure 3: The model can describe a neurovascular response driven by the inhibitory neurons. Data and model simulations for inhibitory optogenetic 5 Hz stimulation (orange), excitatory optogenetic 5 Hz stimulation (blue), sensory electrical stimulation on the inhibitory mice-line (grey), and sensory electrical stimulation on the excitatory mice-line (dark grey). The stimulation duration is indicated by the black bar at the x-axis and is 4 s long (A-E, G, H). Data is originally presented by Vazquez et al. (Vazquez, Fukuda and Kim, 2018) and describe percentual concentration changes ($\Delta\%$) of **A**) oxygenated haemoglobin (HbO), **B**) deoxygenated haemoglobin (HbR), **C**) total haemoglobin (HbT), **D, G-H**) cerebral blood flow (CBF), and **E**) the OIS-BOLD signal. For each graph: the mean experimental data is indicated by an asterisk (*); the standard error of the mean is given by the error bars; the best model simulation is displayed as the solid line; the model uncertainty is given by the coloured semi-

216 transparent overlay, corresponding to a 95 % CI. The sensory data and simulation are shown in the inserted graphs
217 (A-E). The x-axis represents time in seconds. F) The model simulated area under the curve (AUC) for the overall
218 vasoactive effect of NO, inhibitory dilatating vasoactive substance, and PGE₂, excitatory dilating vasoactive
219 substance, are shown for the excitatory and inhibitory simulations. Error bars indicate a 95 % CI for the AUC (F-H).
220 A model validation of blocking the NOS signalling pathway was tested by: G) stimulating with a 5 s long inhibitory
221 5 Hz stimulation and H) a 5 s long sensory electrical stimulation. The bars show the peak amplitude percentage
222 change ($\Delta\%$) in cerebral blood flow. The left bar represents the measured peak amplitude when the NOS pathway
223 is not blocked, corresponding to the data error bars in panel D. The middle bar represents the measured peak
224 amplitude when the NOS pathway is blocked. The right bar represents the model-predicted peak amplitude when
225 the NOS pathway is blocked.

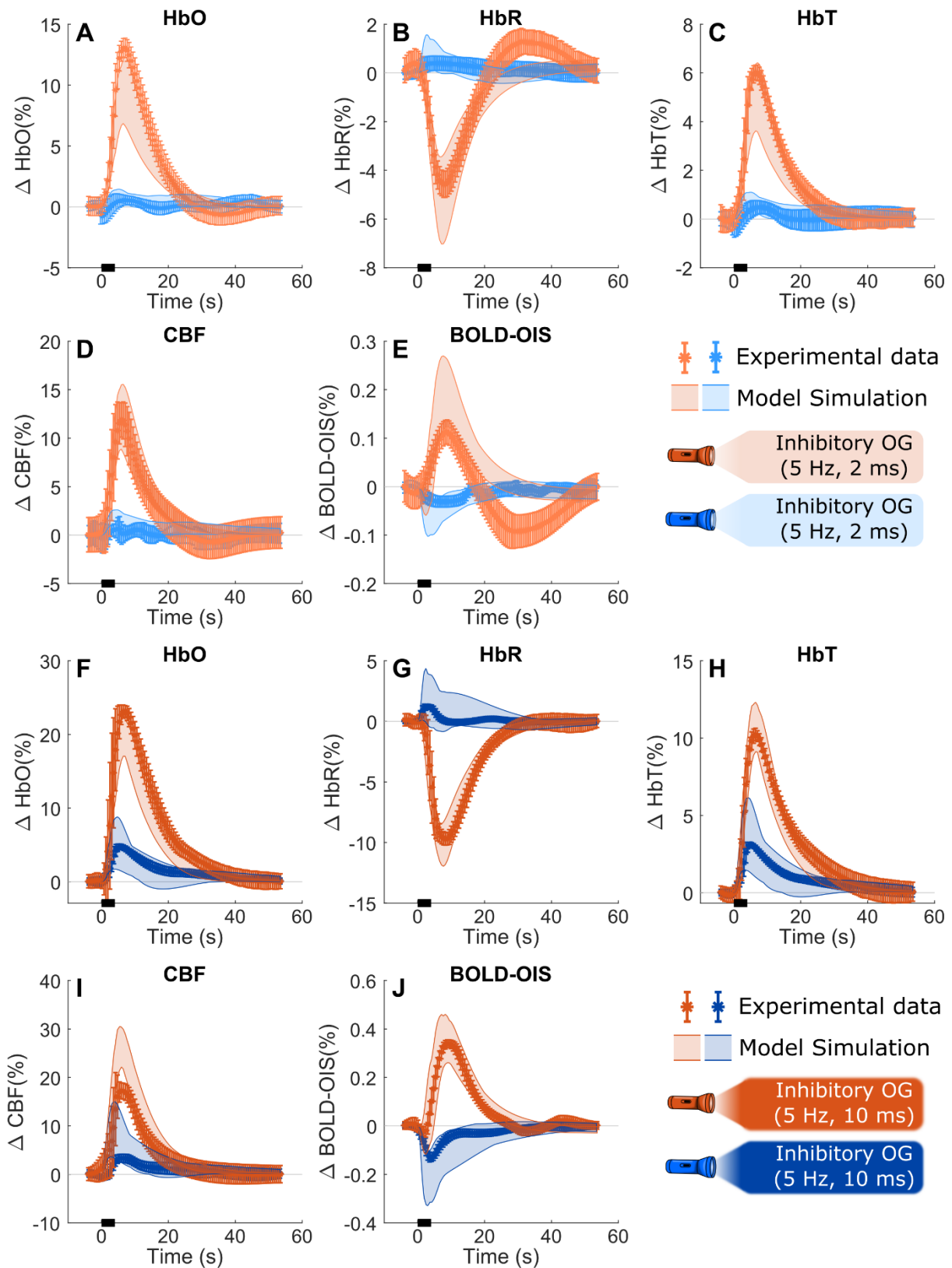
226 A more in-depth analysis of the model shows that NO released from NO-interneurons is the dominant
227 vasoactive agent. Model simulations of the two main vasodilating substances, NO and Prostaglandin E₂
228 (PGE₂), can be seen in Figure 3F, for both excitatory and inhibitory stimulation. As expected, for the
229 inhibitory stimulation, NO is the dominant vasoactive agent (Figure 3F, right). Interestingly, also for
230 excitatory stimulation, NO has a contribution equally big as the PGE₂ contribution (Figure 3F, left).

231 The idea that NO is the primary vasoactive substance is explored by a model validation test, simulating
232 the effects of blocking the nitric oxide synthase (NOS) pathway. The model predicts that the
233 neurovascular response is eliminated (Figure 3G, right) when NOS is blocked, and the cells are exposed
234 to an inhibitory optogenetic stimulation. This model prediction was then compared to data from
235 Vazquez *et al.* where this experiment was done (Figure 3G, middle). As can be seen, the experimental
236 data confirms the model prediction that the NOS-blocked response is almost non-existing (<3 %, Figure
237 3G, middle). A similar validation was done also for NOS being blocked during a sensory stimulation
238 paradigm. Here, the model predicts that the response is slightly higher (0-5 %, Figure 3H, right) which
239 is consistent with the experimental validation experiment (4-6 %, Figure 3H, middle). This low but non-
240 zero response comes from the fact that the sensory stimulation primarily activates the excitatory
241 pyramidal cells, due to the NOS-inhibition. Note that the model has not been trained to any of these
242 NOS-inhibition experiments, thus the model predictions agreeing with these experiments serve as a
243 validation of the model.

244 [The model is validated by its ability to predict new data not used for model training](#)

245 The model was further validated by predicting additional data, presented by Vazquez *et al.* (Vazquez,
246 Fukuda and Kim, 2018), which were not part of the model training and therefore unknown to the
247 model. These model predictions, of optogenetic inhibitory and excitatory stimulation with pulse widths
248 of 2 ms and 10 ms, are in good agreement with data and capture the main features. For instance, the
249 amplitude of the inhibitory HbO response is accurately lowered from 23 % (Figure 4F) to 15 % (Figure
250 4A) for the inhibitory stimulation (orange), comparing pulse widths of 10 ms and 2 ms respectively.

Model Predictions



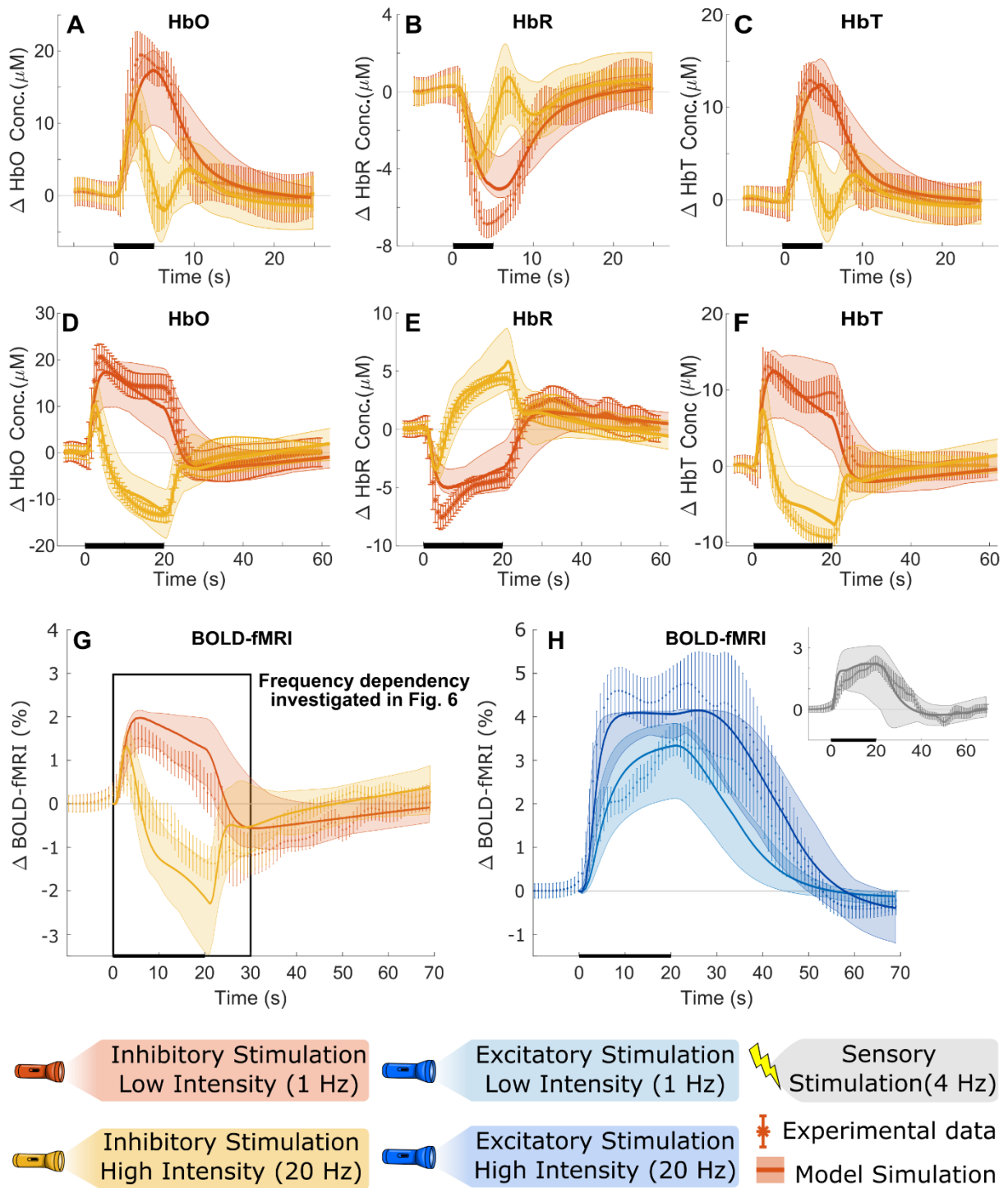
251
252
253
254
255

Figure 4: The model can predict OG data which it has not been trained on. Data and model simulations for optogenetic stimulation with a frequency of 5 HZ and the type: i) inhibitory stimulation with 2 ms pulse width (light orange), ii) excitatory stimulation with 2 ms pulse width (blue), iii) inhibitory stimulation with 10 ms pulse width (orange), and iv) excitatory stimulation with 10 ms pulse width (dark blue). The stimulation duration is

256 indicated by the black bar at the x-axis and is 4 s long (A-J). Data is originally presented by Vazquez et al.
257 (Vazquez, Fukuda and Kim, 2018) and describe percentual concentration changes ($\Delta\%$) of oxygenated
258 haemoglobin (HbO)(A, F), deoxygenated haemoglobin (HbR)(B, G), total haemoglobin (HbT)(C, H), cerebral
259 blood flow (CBF)(D, I), and the OIS-BOLD signal (E, J). For each graph: the mean experimental data is indicated
260 by asterisk (*); the standard error of the mean is given by the error bars; the model uncertainty is given by the
261 coloured semi-transparent overlay, corresponding to a 95 % CI.

262 The model explains how different stimulation frequencies lead to qualitatively different 263 vascular responses

264 The training and validation data used for the model-driven meta-analysis also include data showcasing
265 a frequency-dependent behaviour in response to different optogenetic stimulations. The data,
266 presented by Moon et al. (Moon et al., 2021), are depicted together with our model simulations in
267 Figure 5. This data shows: changes in HbO (Figures 5A and D), HbR (Figures 5B and E), and HbT (Figures
268 5C and F) for a 5 s stimulation (Figures 5A-C) and a 20 s stimulation (Figures 5D-F), including both a low-
269 intensity (1 Hz) inhibitory optogenetic stimulation (orange) and a high-intensity (20 Hz) inhibitory
270 optogenetic stimulation (yellow). Further, the BOLD-fMRI is shown for both inhibitory stimulations
271 (Figure 5G) and for comparison, the BOLD-fMRI response to a: low-intensity (1 Hz) excitatory
272 optogenetic stimulation, high-intensity (20 Hz) excitatory optogenetic stimulation, and a 4 Hz sensory
273 stimulation is shown in Figure 5H. The model simulations (continuous lines and shaded areas) agree
274 well with all the main features seen in the data (error bars). This qualitative assessment was confirmed
275 using a the same χ^2 -test as previously ($f(\theta_{H1}) = 2033.43$, that passed the cut-off threshold,
276 $\chi^2(\alpha = 0.05, Dof = 3347) = 3482.70$).



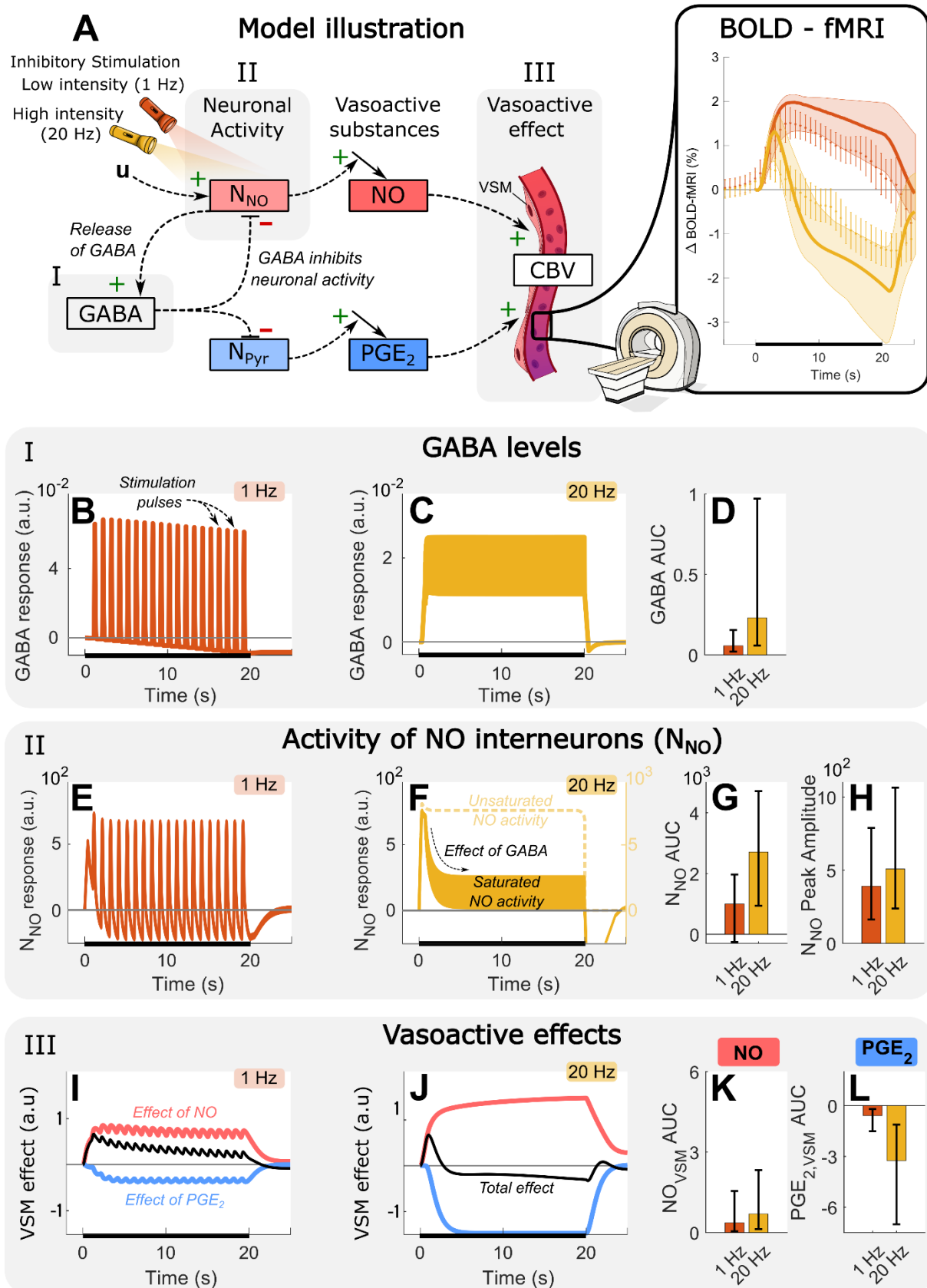
277
 278 **Figure 5: The model can simultaneously describe the qualitatively different responses to the different**
 279 **stimulation intensities.** Data and model simulations for inhibitory optogenetic 20 Hz stimulation (yellow) and
 280 inhibitory optogenetic 1 Hz stimulation (orange). The stimulation duration is denoted by the black bar at the x-
 281 axis, 5 s long (A-C) and 20 s long (D-F). Data was originally presented by Moon et al. (Moon et al., 2021) and
 282 describe the relative concentration changes ($\Delta\mu$ M) of oxygenated haemoglobin (HbO)(A, D), deoxygenated
 283 haemoglobin (HbR)(B, E), and total haemoglobin (HbT)(C, F). Data for BOLD-fMRI for these two inhibitory
 284 stimulations is presented in G). Optogenetic excitatory stimulations were also performed with the same
 285 frequencies, blue 1 Hz and dark blue 20 Hz, and the BOLD-fMRI response is shown in H). The insert shows the
 286 response for a 4 Hz sensory stimulation, grey. For each graph: the mean value of the experimental data is indicated
 287 by an asterisk (*); the standard error of the mean is given by the error bars; the best model simulation is seen as

288 *the solid line; the model uncertainty, corresponding to a 95 % CI, is given by the coloured semi-transparent overlay.*
289 *The x-axis represents time in seconds.*

290

291

292 One of the interesting features seen in both model and data is a biphasic vascular response, i.e. an
293 initial increasing above the baseline, followed by a fall below the baseline (Figure 5G and 6A, yellow).
294 This behaviour is only seen for the high-intensity stimulation, and not seen in the low-intensity
295 stimulation. This difference is not intuitive, as one would generally associate a more intensive
296 stimulation with a stronger and more positive vascular response, compared to the low-intensity
297 response. It is therefore interesting to use the model to understand how this difference can be
298 mechanistically understood.



299
300
301
302
303

Figure 6: The neurovascular dependency on the stimulation intensity is explained by GABA dynamics. A) A simplified model illustration, showing that the stimulation (u) upregulates neuronal activity of NO interneurons (N_{NO}) and pyramidal neurons (N_{Pyr}). The neuronal activity then leads to production of vasoactive substances, NO and PGE_2 . Additionally, N_{NO} initiates the release of GABA, which downregulates all neuronal activity. Thus, the

304 *vasoactive response is a result of the balance between the effect of the stimulation and the inhibitory effect of*
305 *GABA. The biphasic behaviour seen in the Moon et al. (Moon et al., 2021) data is showcased in the box to the*
306 *right, with the 1 Hz stimulation being orange and 20 Hz stimulation being yellow. The simulated model behaviour*
307 *of B) GABA for the 1 Hz and C) 20 Hz stimulation, show that D) the AUC of GABA is larger for the 20 Hz stimulations.*
308 *E) the simulated model behaviour of N_{NO} for the 1Hz stimulation, and F) the 20 Hz stimulation, similarly show that*
309 *the G) area under the curve (AUC) and H) peak value is relatively similar. This would not be the case if the*
310 *stimulation effect was not subject to saturation, F right y-axis. The 1 Hz stimulation produces the vasoactive effect*
311 *in I) where the total effect (black) reflects the dilating effect of NO (red), as the constricting effect from a lack of*
312 *PGE_2 is weaker. J) The 20 Hz stimulation results in a net vasoconstricting effect (black curve below baseline) due*
313 *to a more substantial lack of PGE_2 which cancels out the dilating effect of NO. Notably, the increase K) of NO levels*
314 *is not as big compared to the loss L) of PGE_2 comparing the high- and low-intensity stimulations. Error bars indicate*
315 *a 95 % CI.*

316 The model explains the biphasic response observed for the high-intensity stimulation as a balance
317 between a saturated inhibitory neuronal activity, and elevated levels of GABA. The optogenetic
318 stimulation (u) excites the NO-interneurons and GABA is released, which in turn inhibits all neuronal
319 activity (Figure 6A, N_{NO} and N_{Pyr}). For the high-intensity stimulation, there is not enough time between
320 stimulation pulses for the GABA levels to return to baseline (Figure 6C), resulting in overall elevated
321 levels of GABA (Figure 6D), compared to the low-intensity stimulation (Figure 6B). Simultaneously, the
322 activity of the NO-interneurons (N_{NO}) is subjected to a saturation effect (Equation 7) which, together
323 with the elevated GABA levels, results in the overall neuronal activity being very similar between the
324 high- and low-intensity stimulations (Figure 6G, H). Although the bursting of neuronal activity settles at
325 a lower amplitude for the high-intensity stimulation (due to the elevated GABA levels), the resting
326 activity between spikes does not fall below the baseline (Figure 6F). Consequently, the stimulation
327 intensity has no discernible effect on the peak amplitude of N_{NO} (Figure 6H) and only a slight effect on
328 the overall levels of neuronal activity (Figure 6G). Subsequently, the vasodilating effect of the NO-
329 release remain similar between the stimulations. This can be seen both in the amplitude of NO's
330 vasoactive effect (Figure 6I-J, red) and the overall AUC of NO's vasoactive effect (Figure 6K). As for the
331 pyramidal neurons, their activity (N_{Pyr}) is inhibited by GABA (Figure 6A), causing a decreased release of
332 vasodilating PGE_2 (Figures 6I-J, blue). Due to the elevated levels of GABA during the high-intensity
333 stimulation, the vasoactive effect of PGE_2 is reduced substantially more (Figure 6J, blue), compared to
334 the low-intensity stimulation (Figure 6I, blue). Since both NO and PGE_2 have vasodilating properties,
335 the comparatively greater reduction of PGE_2 (Figure 6L), compared to the modest increase of NO
336 (Figure 6K), causes a net contraction of the blood vessels after an initial dilation (Figure 6J, black). This
337 dynamic results in the biphasic response seen for the high-intensity stimulation (Figure 6A, yellow).
338 The biphasic response is not present during the low-intensity stimulation due to the increase of NO
339 offsetting the reduced levels of PGE_2 , resulting in a net dilation of the blood vessels (Figure 6A, orange).

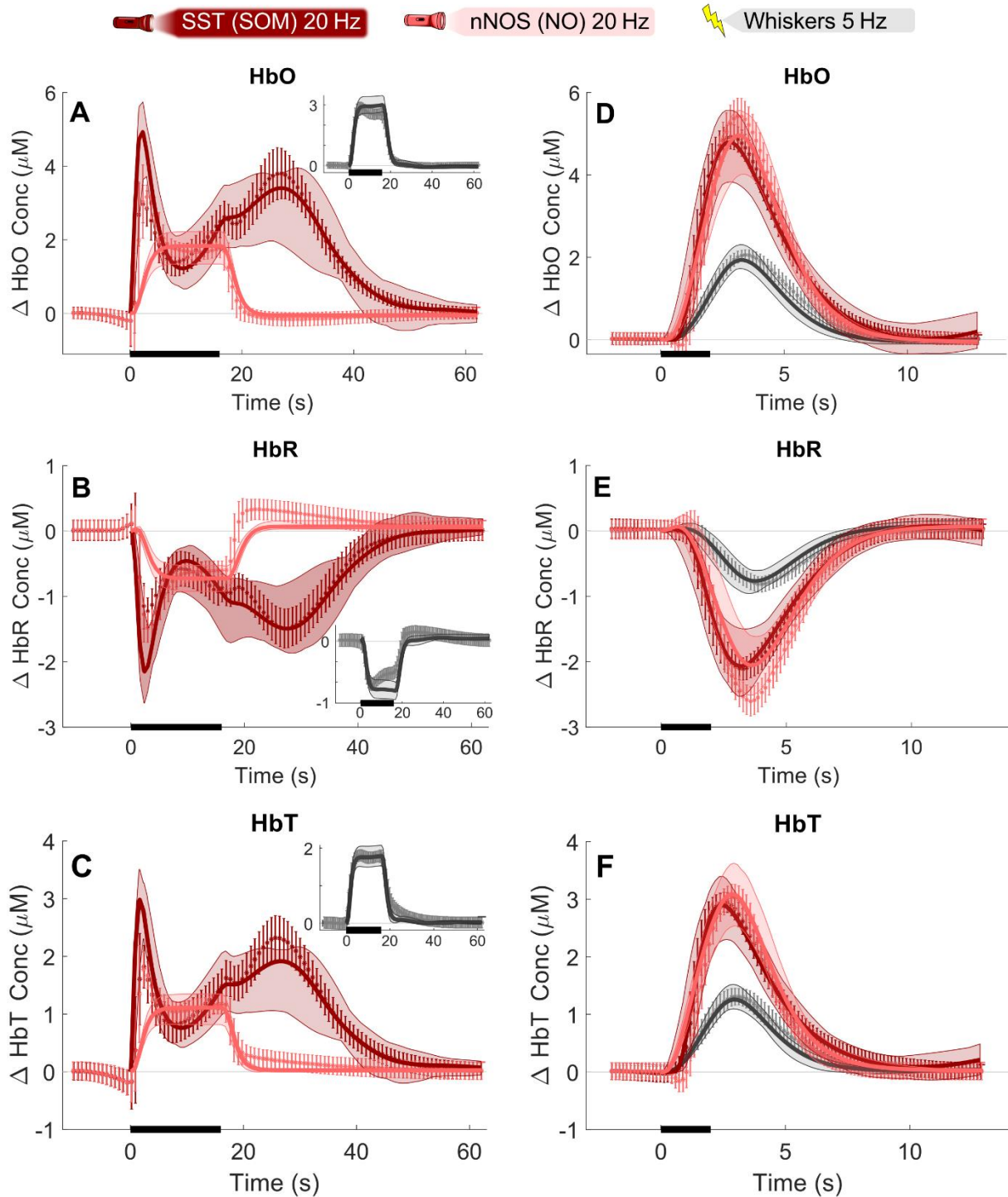
340 It should be noted that the saturation of neuronal activity seems to be a crucial mechanism, without
341 which the model is not able to describe the biphasic response accurately. In the model, this saturation
342 is implemented by limiting the degree to which the optogenetic stimulation can stimulate the model
343 state that represents the neuronal activity. This means that during high-intensity stimulation this model
344 state will reach a stable plateau and additional stimulation will not increase the neuronal activity
345 further (Figure 6F, see Methods for details). Without this saturation effect, the peak amplitude of N_{NO}
346 would increase by an order of magnitude during the high-intensity stimulation (Figure 6F, right y-axis),
347 resulting in much more NO being released and an increased vasodilating effect. This increased

348 vasodilation would counteract the decreased levels of PGE₂, resulting in net vasodilation, and the
349 biphasic response would not be observed.

350 The biphasic behaviour is not present when observing a similar setup using excitatory optogenetic
351 stimulation (Figure 5H). In this case, we see the high-intensity (dark blue) stimulation produces a faster
352 and stronger response compared to the low-intensity (blue) stimulation. While this scenario seems
353 similar to the inhibitory stimulation at first glance, the underlying interactions differ. Activating the
354 pyramidal neurons release glutamate which subsequently activate the interneurons and triggers the
355 release of GABA. Crucially, this means that a balance between excitatory and inhibitory neuronal
356 activity is achieved for both the high- and low-intensity excitatory stimulations. This alters the tug-of-
357 war between neuronal activation and inhibition that we saw for the inhibitory stimulation, and the
358 vascular response instead intuitively scales in proportion to the stimulation intensity. Note that the
359 simulation of neuronal activity is still subject to the saturation effect discussed above.

360 The role of Somatostatin releasing neurons in the NVC

361 Finally, we investigate the role of somatostatin (SOM)-releasing interneurons in the neurovascular
362 response, using an expanded model structure which also included SOM-interneurons. This analysis was
363 based on data presented by Lee *et al.* (Lee *et al.*, 2020) and includes: the relative changes in HbO
364 (Figures 7A and D), HbR (Figures 7B and E), and HbT concentrations (Figures 7C and F) in response to
365 20 Hz optogenetic stimulations of SOM releasing interneurons (Figure 7, crimson), of NO-interneurons
366 (Figure 7, light red), as well as sensory stimulation (Figure 7, grey). Two stimulation lengths were
367 evaluated, 16 sec (Figures 7A-C) and 2 sec (Figures 7 D-F). The model simulations (lines) agree with all
368 the main features seen in the data (error bars). The qualitative assessment was again confirmed using
369 a χ^2 -test (Equation 11; $f(\theta_{H1}) = 1013.46$ which is lower than the cut-off threshold $\chi^2(\alpha =$
370 $0.05, Dof = 1548) = 1640.65$).



371
 372 **Figure 7: The model can describe a delayed dilation using somatostatin-releasing interneurons.** Data and model
 373 simulations for inhibitory nNOS 20 Hz stimulation (light red), inhibitory SST 20 Hz stimulation (crimson), and
 374 sensory whiskers 5 Hz stimulation (grey). The stimulation duration is denoted by the black bar at the x-axis and is
 375 16 s long (A-C) and 2 s long (D-F). Data was originally presented by Lee et al. (Lee et al., 2020) and describe the
 376 relative concentration changes ($\Delta\mu$ M) of oxygenated haemoglobin (HbO) (A, D), deoxygenated haemoglobin
 377 (HbR) (B, E), and total haemoglobin (HbT) (C, F). For each graph: the mean value of the experimental data is
 378 indicated by an asterisk (*); the standard error of the mean is given by the error bars; the best model simulation
 379 is seen as the solid line; the model uncertainty corresponding to a 95 % CI is given by the coloured semi-
 380 transparent overlay. The sensory data and simulation are shown in the inserted graphs for the long stimulation
 381 (A-C). The x-axis represents time in seconds.

382 The data show that selectively stimulating SOM-interneurons gives rise to a double-peak response in
383 the Hb measurements (Figures 7A-C, crimson), which is not present for the NO-stimulation (light red),
384 nor for the sensory stimulation (Figures 7A–C, inserts). The model can accurately describe the observed
385 double peak dynamic in response to stimulating SOM neurons, given that a corresponding signalling
386 pathway is introduced to the model structure (Figure 8). We found that the mechanism of this double-
387 peak dynamic has two main components: a) the initial peak is generated by the direct vasoactive
388 influence of the SOM-releasing neurons; b) the second peak is generated by a delayed recovery from
389 the inhibition of activity in the other neuron populations (NO, NPY, and Pyramidal neurons). A detailed
390 analysis of this double peak response can be found in the Supplementary Materials (Supplementary
391 Materials section 2).

392 Discussion

393 This work investigates the different contributions of inhibitory and excitatory neurons to the
394 neurovascular response using experimental data from several different studies in a model-driven meta-
395 analysis. This approach allows us to generate quantitative estimates for the cell-type-specific
396 contributions to the fMRI-BOLD-signal. Our analysis shows that the inhibitory neurons are the biggest
397 contributors to the BOLD-response (Figures 2A and D) in 8 of the 11 experiments (Vazquez, Fukuda and
398 Kim, 2018; Lee *et al.*, 2020; Moon *et al.*, 2021), and always the biggest contributor to the vascular
399 response (Figure 2C). Furthermore, the mode-based analysis accurately describes the key qualitative
400 dynamics observed in data (Figures 3, 6, and S3), and correctly predict new validation data not used for
401 model training: the response to NOS-inhibition (Figure 3G), and a 2 ms and 10 ms pulse width
402 stimulation paradigm (Figure 4). Importantly, the model could describe how the inhibitory neurons act
403 as the primary contributors to the regulation of the vascular response (Figure 3). Furthermore, the
404 model was able to explain why high-intensity, but not low-intensity, stimulations of interneurons lead
405 to a biphasic BOLD-response (Figure 6): it is because the stimulation of NO-interneurons (Figure 6G) is
406 balanced out by GABA (Figure 6D), while strongly inhibiting the pyramidal cells, causing a net
407 vasodilation (Figure 6J, black) as the release of NO (Figure 6K) cannot offset the lack of PGE₂ (Figure
408 6L). Finally, we could use the model to explain why there is a double-peak in response to prolonged
409 SOM stimulations (Figure 7A, crimson): a) the initial peak is generated by the direct vasoactive influence
410 of the SOM-releasing neurons; b) the second peak is generated by a delayed recovery from the
411 inhibition of activity in the other neuron populations (NO, NPY, and Pyramidal neurons)(Supplementary
412 Materials section 2). In summary, our results provide a detailed, quantitative, and mechanistic
413 underpinning for a new consensus view across 11 different experiments: that it is interneurons and not
414 pyramidal cells that dominate the BOLD response.

415 Other models investigating the neurovascular coupling

416 Various studies have developed different types of mathematical models to investigate the NVC (Griffeth
417 and Buxton, 2011; Havlicek *et al.*, 2015; Kim and Ress, 2016; Lundengård *et al.*, 2016; Di Volo *et al.*,
418 2019; Sten *et al.*, 2020, 2023; Moon *et al.*, 2021; Tesler, Linne and Destexhe, 2023). However, very few
419 studies have investigated the more prominent role of inhibitory neuron populations suggested by
420 recent experimental results. Firstly, the work by Moon *et al.* 2021 describe a 2-pole, 1-zero Laplace
421 function, which primarily focuses on capturing the qualitative temporal features of the so-called
422 hemodynamic response function (HRF)(Moon *et al.*, 2021). However, this model offers no mechanistic
423 insights into the neurovascular response. Secondly, Tesler *et al.* proposes a model that describes the
424 contribution of astrocyte calcium dynamics to the relationship between neuronal activity and the fMRI-
425 BOLD response (Tesler, Linne and Destexhe, 2023). This work uses a mean-field neuron spiking model
426 (Di Volo *et al.*, 2019) to describe selective activation of excitatory and inhibitory neurons. The Tesler
427 model is limited by only having the astrocytes, thus not including the prominent effect of NO,
428 controlling CBF and primarily focusing on excitatory neuronal stimulation. Lastly, our own prior work
429 (Sten *et al.*, 2023) presents a model including both inhibitory and excitatory neurons that could
430 describe neurovascular control in response to different stimulation types, including optogenetic
431 stimulations. Similarly to the other mentioned models, the Sten model predominantly focuses on
432 excitatory neuronal stimulation as a main contributor to the regulation of CBF. As such, to the best of
433 our knowledge, no studies are using state-of-the-art mechanistic models to investigate the qualitative
434 differences (Figures 3-7, S3) of inhibitory neuronal populations to NVC, and no previous analysis has

435 been able to quantify the cell-specific quantitative contributions to the BOLD, CMRO₂, HBR, and CBV
436 responses (Figures 2, S1-S2) to the NVC.

437 [Model explanation of key qualitative behaviours in data](#)

438 Our model analysis, based on our mechanistic mathematical model (Figure 8), provides a cohesive
439 framework to investigate the different qualitative behaviours seen in the experimental data. We
440 present such explanations for: 1) the dominant neurovascular control of inhibitory neurons (Figure 3);
441 2) the biphasic response observed for high-intensity inhibitory stimulation (Figure 6); 3) the emergence
442 of a double-peak behaviour stimulation SOM-interneurons (Figure S3).

443 To the first point, the dominant control of inhibitory neurons, our model captures this behaviour well
444 over different data (Figure 3A-E). The simulations capture the prominent features in data: a peak value
445 occurring roughly 9 seconds after the stimulation has ceased (0-4 sec), followed by a return to baseline.
446 While explaining the change in HbO, HbR, HbT, and OIS-BOLD well (Figures 3A-C, E, orange), the model
447 slightly overshoots the CBF response (Figure 3D, orange). Similarly, the model captures the more
448 modest responses generated from the excitatory optogenetic stimulation (Figures 3A-E, blue). The
449 model also captures the qualitative difference in HbR-dynamics between the different stimulations,
450 i.e. decreasing during inhibitory stimulation and increasing during excitatory stimulation. The increase
451 in HbR is attributed to a combination of a high metabolic load and a relatively weak vascular response
452 (Figure 3D, blue). Model analysis reveals that the higher metabolic load is attributed to the stimulation
453 of excitatory neurons, which have a greater contribution to CMRO₂ (Figures 2B, S1)(Meyer *et al.*, 2011)
454 These different HbR-responses are also mirrored in the OIS-BOLD response (Figure 3E). Additionally,
455 for the sensory stimulation (Figure 3, inserts), in which both the inhibitory and excitatory pathways are
456 activated, we see again that the inhibitory neurons contribute the main part of the vascular response
457 (Figures S1-S2, Exp. 2 and 3).

458 Secondly, our analysis of the stimulation-intensity-dependent biphasic behaviour (Figure 6), also
459 suggests a distinct temporal hierarchy in neuronal activation. We observe a very rapid response from
460 the NO-interneurons (Figure 6I and J, red); followed by a slightly delayed activation of the pyramidal
461 neurons, which release PGE₂ (Figure 6I-J, blue); and lastly by the considerably slower response NPY-
462 interneurons. This dynamic of neuronal activation aligns well with the HRF-model presented by Moon
463 *et al.*, which describes both the fMRI-BOLD and HbR responses with a fast-acting inhibitory component
464 and a slower-acting excitatory component (Moon *et al.*, 2021). Additionally, the same temporal
465 hierarchy of neuronal activation was also observed in our previous work (Sten *et al.*, 2023), where this
466 dynamic could be preserved across multiple experiments in different species. This alignment across
467 different research efforts underscores the foundational nature of this temporal hierarchy. Moreover,
468 our model extends these insights by offering a more detailed mechanistic explanation of the processes
469 involved. Additionally, the stimulation-intensity-dependent model explanation also aligns with recent
470 experimental findings presented by Dadarlat *et al.*, where they also observe that the level of
471 stimulation intensity affects the response of the inhibitory neurons (Dadarlat, Sun and Stryker, 2024).

472 Thirdly, the emergence of a double-peak behaviour, seen in Figure 7, is associated with the stimulation
473 of SOM-interneurons (Lee *et al.*, 2020). The double-peak dynamic could be explained by the SOM-
474 interneurons having slower intracellular pathways, compared to NO-interneurons (Figure S3,
475 Supplementary Materials section 2). Moreover, the model simulation suggests that the double-peak
476 dynamic is attributed to a reduction and recovery of the vasoconstrictor NPY. In our previous work (Sten
477 *et al.*, 2023), we put forward another mechanism for describing the double-peak behaviour presented

478 by Drew *et al.* (Drew, Shih and Kleinfeld, 2011). However, this previous explanation relied on the
479 excitatory neurons acting as the primary driver of the neurovascular response. The data analysed in
480 this work (Vazquez, Fukuda and Kim, 2018; Lee *et al.*, 2020; Moon *et al.*, 2021) do not support this
481 excitatory-driven explanation. Instead, the current work puts forth an explanation where the inhibitory
482 neurons are the main contributor to the neurovascular response.

483 Model analysis limitations and critical features in data

484 The model analysis is limited to the information contained in the training data. The analysed
485 optogenetic data are gathered from a range of varying experimental protocol parameters, see
486 Supplementary Table 1, where stimulation strength, duration, frequency, and anaesthesia dosing
487 protocol differ. Our framework attempts to analyse these data collectively to investigate how these
488 differences relate to the experiments. This means that the analysis is subject to some limiting features
489 presented in the experimental protocol and contradictory behaviour in the resulting data.

490 One example of contradictory behaviour are the Hb responses to stimulating the NO-interneurons in
491 Lee *et al.* (Figure 7, light red)(Lee *et al.*, 2020), compared with the high-intensity stimulation of NO-
492 interneurons (Figure 5, yellow)(Moon *et al.*, 2021). These experiments share similar stimulation
493 protocol parameters (Supplementary Table 1) and therefore one would expect similar vascular
494 responses. However, the Hb dynamics differ greatly and most notable is that the biphasic response is
495 missing from the Lee *et al.* NO-response. Instead, the NO-response is qualitatively closer to the 1 Hz
496 stimulation response presented by Moon *et al.* (Figure 5, orange). It should be noted that these studies
497 use different optogenetic lines (NOS-connected pathway in Lee *et al.* and vesicular GABA transport
498 (VGAT) vectors in Moon *et al.*) to introduce the light-sensitive Channelrhodopsin-2 (ChR2) ion channels
499 into the mice. While this choice of vector could be expected to cause some differences in the vascular
500 responses, one would not expect such qualitatively different responses. Rather, these differences in
501 responses could be attributed to the data being recorded in different brain areas and/or different
502 anaesthesia protocols being used.

503 Factors that affect the stimulation and how the stimulation is perceived by the cells, e.g. anaesthesia
504 protocol, could contribute to the qualitative different response seen across the three analysed studies
505 (Vazquez, Fukuda and Kim, 2018; Lee *et al.*, 2020; Moon *et al.*, 2021). For example, when observing
506 the overall light exposure per second for each study, analysis reveal that all optogenetic experiments
507 employ 150-200 ms of light exposure per second (Supplementary Table 1). However, these similar light
508 exposures cause widely different neurovascular responses (Figures 3-7) and the differences probably
509 lie in how the electrophysiological activity responds to the different stimulation protocols. For instance,
510 to explain the frequency-dependent response seen in Figure 6 we needed a stimulation saturation
511 effect. Such a mechanism could be connected to the recovery phase present in electrophysiological
512 models, i.e. the hyperpolarization phase of neuronal ion channels (Tsodyks and Markram, 1997;
513 Rosenbaum, Rubin and Doiron, 2012) and global depressive phases of neuronal networks (Zhang *et al.*,
514 2016). These systems actively regulate themselves to avoid overstimulation and our model analyses
515 indicate a similar role for GABA (Figure 6D). Furthermore, it has been shown that the anaesthesia itself
516 influences NVC dynamics (Uhlirva *et al.*, 2016). We have previously presented a modelling approach
517 to investigate the anaesthesia effect on the vascular control (Sten *et al.*, 2020). However, to the best of
518 our knowledge, no such investigation has yet been performed on the electrophysiological properties in
519 response to the optogenetic stimulation. If one were to analyse the interaction of anaesthesia and

520 optogenetic stimulation in *in silico* spiking neuronal network models (Lee, Wang and Hudetz, 2020; H.
521 Lee *et al.*, 2021), one could potentially find explanations for the observed vascular differences.

522 We should note that our model structure does not attribute any vascular control to the astrocytes,
523 instead they only contribute to the metabolism. As the model was iteratively developed (Figure 1D),
524 the astrocytes were initially included solely to regulate the levels of glutamate and GABA, and
525 subsequently the activity of the neurons. However, the model also required the metabolic
526 contributions of the astrocytes to accurately explain the data, while their direct vascular regulation
527 could still be assumed to be negligible. This does not necessarily mean that the astrocytes'
528 contributions to vascular regulation are negligible, only that the current model structure could explain
529 the considered data given this assumption. This assumption stands in contrast to other modelling
530 frameworks, such as Tesler *et al.* (Tesler, Linne and Destexhe, 2023), that do include astrocytes with an
531 active role in vascular control. Similar assumptions have also been made for other interactions between
532 the astrocytes and neurons.

533 Lastly, we acknowledge limitations in the level of detail of our neural model that could be addressed to
534 improve our predictions. For example, the model only includes one type of excitatory (pyramidal) and
535 three types of inhibitory neurons (SOM, NPY, NO), but other known neuron types and subtypes such
536 as interneurons expressing parvalbumin (PV) or vasoactive intestinal peptide (VIP), may play important
537 roles in NVC (Krogsgaard *et al.*, 2023; Yao *et al.*, 2023). Additionally, the modelled spatial distribution
538 and synaptic connectivity of neurons is currently overly simplified, and omits, for example, the six layer
539 cortical structure and complex interlaminar and long-range connectivity patterns (Harris and Shepherd,
540 2015). These spatial and connectivity properties may have important implications for calculating NVC
541 responses, as local neural activity may trigger strong responses in distally connected neural
542 populations. Polysynaptic inhibitory connectivity patterns, such as disinaptic inhibition (E->I->E) and
543 disinhibition (I->I->E), may be important to interpret the contribution of inhibitory activity in the BOLD
544 response. We are working towards extending our analysis using data-driven multiscale biophysical
545 circuit models that incorporate known cell types, anatomical structure and synaptic connectivity (Dura-
546 Bernal *et al.*, 2019; Dura-Bernal, Griffith, *et al.*, 2023; Dura-Bernal, Neymotin, *et al.*, 2023).

547 [An emerging consensus view that inhibitory neurons dominate the vascular and BOLD](#) 548 [response: arguments for and against](#)

549 The result of this work primarily argues for a new consensus view that inhibitory neurons, and not
550 pyramidal neurons, are the most dominant cell type in generating vascular and BOLD responses. We
551 have quantified the contribution of the different cell types and found that interneurons dominate the
552 BOLD response in 8 out of 11 experiments, and the vascular response in all 11 experiments (Figure 2).
553 Furthermore, we have provided an extensive mechanistic underpinning for how this new role of
554 interneurons can be used to explain various details in responses, such as a biphasic response to high-
555 intensity interneuron stimulation (Figure 6), and a double-peak response to prolonged SOM stimulation
556 (Figure 7). All of these results argue for a new and more prominent role of interneurons, which is
557 compatible with many new studies (Vazquez, Fukuda and Kim, 2018; Echagarruga *et al.*, 2020; Moon
558 *et al.*, 2021). However, it should also be noted that other, and contradictory results, also have been
559 reported. For instance, studies on excitatory neuron stimulation show both a modest (Vazquez *et al.*,
560 2014; Vazquez, Fukuda and Kim, 2018) versus prominent (Desjardins *et al.*, 2019; J. Lee *et al.*, 2021;
561 Moon *et al.*, 2021) hemodynamic responses. It has also been shown that optogenetic excitatory
562 stimulation can yield a stronger neurovascular response compared to optogenetic inhibitory

563 stimulation (Desjardins *et al.*, 2019). In summary, it is thus clear that our work provides a step towards
564 forming a new consensus view, but that further work needs to be done to get a view that truly
565 encompasses all the seemingly contradictory data.

566 Method

567 To analyse the different dynamics of the NVC that are not unified with the conventional interpretation
568 of vasoactive regulation, a mechanistic mathematical model has been used. This type of model allows
569 for greater integration of experimental data from multiple different studies, considering multiple
570 different variables such as OIS-BOLD, fMRI-BOLD, and Hb levels. The model developed in this study
571 consists of ordinary differential equations (ODEs) and differential algebraic equations (DAEs) and has
572 been formulated to describe the mechanisms involved in the NVC. Parameter estimation, identifiability,
573 and model observability analyses were performed, and the model has been evaluated with respect to
574 its ability to accurately describe different sets of experimental data. These analyses are described in
575 detail in this section.

576 Model formulation

577 The model used in this work is formulated as a system of ODEs and DAEs and can in general be
578 formulated as:

$$\dot{x} = f(x, h, \theta, u, t) \quad (1a)$$

$$x_0 = x(\theta, u, t = 0) \quad (1b)$$

$$0 = h(x, \dot{x}, \theta, t) \quad (1c)$$

$$h_0 = h(x, \dot{x}, \theta, t = 0) \quad (1d)$$

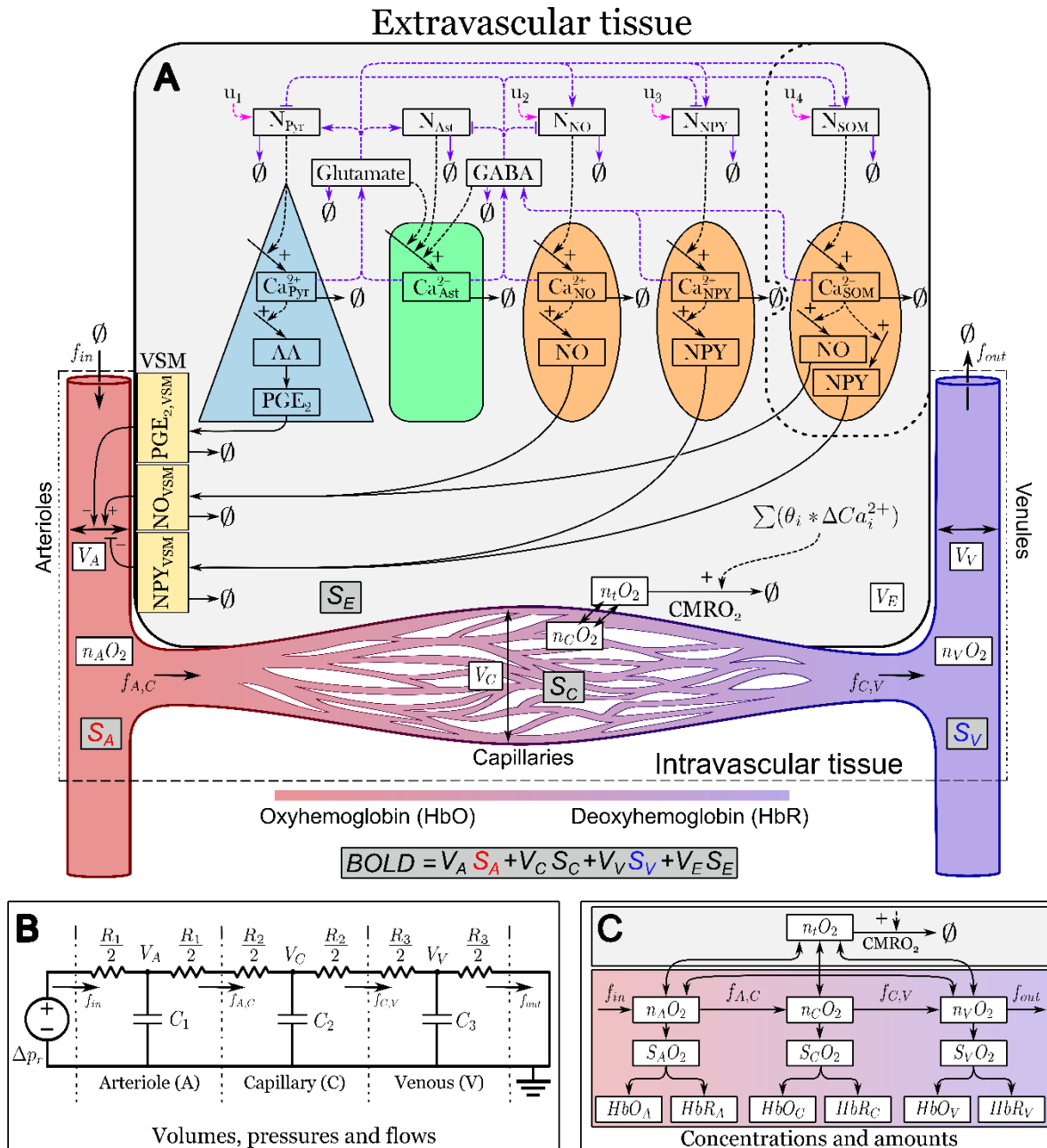
$$\hat{y} = g(x, h, \theta, u, t) \quad (1e)$$

579

580 where x is a vector containing the model states that can be derived with respect to time t ; \dot{x} are the
581 derivatives of states x with respect to t ; x_0 is the values of the states x at the initial timepoint $t = 0$; θ
582 is a vector with the model parameters; u specifies the model inputs; f , h , g are non-linear smooth
583 functions; f describes how the derivatives of the states x change over time with respect to the current
584 value of x , the parameters θ , and the input u ; h describes the system of differential equations and
585 algebraic equations that have no corresponding time derivatives; h_0 are the initial values of the
586 algebraic expressions at time point $t = 0$; and \hat{y} is a vector of the model's observable properties which
587 is described by the function g .

588 Model structure

589 The model used in this study is derived from the model presented in our previous work (Sten *et al.*,
590 2023). This section will give a brief description of this model structure and a detailed description of
591 what changes have been made to the model structure for the work presented herein. For a detailed
592 description of the original model please see the original publication (Sten *et al.*, 2023) and the
593 Supplementary Materials section 5.



594

595

596

597

598

599

600

601

602

603

604

605

606

607

608

Figure 8: An interaction graph of the model structure. **A)** the model represents different types of neurons and glia cells, excitatory pyramidal neurons (blue), activity-regulating astrocytes (green), inhibitory GABAergic nitric oxide (NO), neuropeptide-Y (NPY), and somatostatin (SOM) releasing neurons (orange). These neurons, represented by the states N_{PYT} , N_{NO} , N_{NPY} , and N_{SOM} , can be excited with an external stimulation, $u_{i=\{1,2,3,4\}}$. The excitation is unique to every unique stimulation configuration, indicated by the pink-coloured arrows. When excited the pyramidal neurons increase the level of intracellular calcium ions (Ca_{PYT}^{2+}). The calcium level controls the release of neurotransmitters and the activity of intracellular synthesis of vasoactive substances. The neurotransmitters released are excitatory glutamate, by pyramidal neurons, and inhibitory GABA, by GABAergic interneurons. These neurotransmitters act on the other neurons and are regulated by the astrocytes, which can both synthesize glutamate and GABA dependent on their level of intracellular calcium ions (Ca_{Ast}^{2+}). The purple-coloured arrows indicate that these signalling pathways are allowed to vary due to the anaesthesia conditions differing between different studies. The intracellular calcium is controlled by the neuronal activity of the neurons. The intracellular pathways of the excitatory and inhibitory neurons end with the release of vasoactive substances that influence the vascular smooth muscles (VSM) surrounding the arterioles. Pyramidal neurons release the

609 *vasodilating substance Prostaglandin E2 (PGE₂), NO neurons release the vasodilating substance NO, NPY neurons*
610 *release the vasoconstricting substance NPY, and SOM neurons release both the vasodilating substance NO and*
611 *vasoconstricting substance NPY. The dilation and constriction of the arterioles control the rate of blood entering*
612 *the arterioles. A generalized expression of removal or breakdown is denoted with \emptyset . Further, the vascular*
613 *compartment of the model describes the volume ($V_{i=\{A,C,V,E\}}$), blood flow ($f_{i=\{in,AC,CV,out\}}$), oxygen content*
614 *($n_i O_2, i = \{a, c, v, t\}$), and cerebral metabolic rate of oxygen (CMRO₂) of the arterioles (A), capillaries (C), venules*
615 *(V), tissue (t), and extravascular volume (E). The compartmental volume and oxygen saturation are used to*
616 *calculate the functional magnetic resonance imaging blood oxygen-level dependent (fMRI-BOLD) signal. The total*
617 *fMRI-BOLD signal is the sum of the signal from each compartment ($S_{i=\{A,C,V,E\}}$) **B**) The three-compartment*
618 *vascular model, consisting of arterioles (A), capillaries (C), and venules (V), describes the blood volumes (V_i),*
619 *pressures, and flows (f_i) corresponding to an analogue electrical circuit. The drop in blood pressure over a*
620 *compartment can be represented by a voltage drop, the blood flow is represented by an electric current, and the*
621 *blood volume can be seen as an electric charge stored in capacitors. The vessel compliance ($C_{i=\{1,2,3\}}$) is*
622 *represented by the capacitance of the capacitors, and the vessel resistance ($R_{i=\{1,2,3\}}$) is analogous to the electric*
623 *resistance. The blood pressure difference (ΔP_i) maintained by the intracranial pressure corresponds to the*
624 *electromotive force created by a voltage source. **C**) The oxygen transport model depicts the amount of oxygen*
625 *($n_i O_2$), oxygen saturation ($S_i O_2, i = \{A, C, V\}$), oxygenated haemoglobin ($HbO_{i=\{A,C,V\}}$) and deoxygenated*
626 *haemoglobin ($HbR_{i=\{A,C,V\}}$), for each respective compartment. The rate of oxygen metabolism, which occurs in*
627 *the extravascular tissue, is regulated by the activity of intracellular Ca²⁺ transportation in the different neurons*
628 *(pyramidal, astrocyte, NO-, NPY-, SOM-interneurons). Oxygen diffusion from the vessel compartments to the*
629 *extravascular tissue is concentration-driven. Additionally, oxygen can diffuse from the arterioles to the venules.*
630 *The amount of oxygen can be translated into oxygen saturation ($S_i O_2$), from which the level of oxygenated (HbO_i)*
631 *and deoxygenated blood (HbR_i) can be estimated.*

632

633 Expansion of the Sten *et al.* 2023 model

634 The original model presented in Sten *et al.* 2023 was expanded to accurately explain the experimental
635 data considered herein. These expansions include but were not limited to, an addition of a readout for
636 the OIS-BOLD signal, an expanded expression for the oxygen permeability of the blood vessels and
637 tissue uptake of oxygen, and the introduction of saturated neuronal activity. These additions to the
638 model are detailed in the sections below.

639 Addition of BOLD OIS signal

640 The OIS-BOLD signal was implemented in the model as an exponential expression of the relative change
641 in HbR and CBV levels. The HbR component represents the approximation of the OIS-BOLD signal as an
642 inverse measurement of the change in HbR. The volume-based offset was introduced to account for
643 the light scattering effect caused by an increased blood volume, i.e. an increased blood volume leads
644 to increased light scattering which means a decrease in optical signal. This relationship is explained by
645 the following expression:

$$BOLD\ OIS = \exp(-k_{BOLD} * (HbR - HbR_{SS}) - k_{BOLD2} * (CBV - CBV_{SS})) \quad (2)$$

646 where k_{BOLD} and k_{BOLD2} are scaling parameters which are estimated from data; HbR is the calculated
647 levels of deoxygenated haemoglobin; CBV is the calculated cerebral blood volume; and HbR_{SS} and
648 CBV_{SS} are the baseline values of HbR and CBV, respectively.

649 Oxygen permeability and tissue oxygen uptake

650 The original model had a simplified explanation of the blood vessels' oxygen permeability and tissue
651 oxygen uptake. This expression needed to be expanded for the model to describe the data since the
652 simulated values for the increases in CBF and relative change in HbO did not quite reflect the observed
653 changes in the data (Vazquez, Fukuda and Kim, 2018). This expanded expression for the oxygen
654 permeability was implemented as two separate mechanisms from the model presented by Barret *et al.*
655 2015 (Barrett and Suresh, 2015) the first mechanism represents a dynamic permeability of the capillary
656 vessels, formulated as:

$$g_2 = g_{2,ss} * (1 - k_{capPerm} * [f_0 - f_{0,ss}]) \quad (3)$$

657 where g_2 is the permeability of the capillary vessels; $g_{2,ss}$ is the permeability at baseline; $k_{capPerm}$ is
658 a scaling parameter; f_0 is the blood flow entering the local region; and $f_{0,ss}$ is the blood flow at baseline.

659 The second mechanism describes the effect of recruiting upstream oxygen i.e., the mechanism
660 introduces a “leakage” of oxygen from the blood to other tissue before reaching the brain. In the
661 original model, this leakage is considered to be constant for the duration of the stimulation. In the
662 updated model a dynamic leakage is implemented as:

$$C_{o_2,leak} = \max(C_{o_2,leak,ss} * [1 - k_{leak} * (f_0 - f_{0,ss})]) \quad (4)$$

663 Where $C_{o_2,leak}$ is the loss of O₂ concentration due to “leakage”; $C_{o_2,leak,ss}$ is the leakage at baseline;
664 k_{leak} is a scaling parameter; and f_0 and $f_{0,ss}$ is the blood flow and basal blood flow as described above.
665 The $\max(x, 0)$ function is to prevent a negative O₂ leakage i.e., the blood entering the local region of
666 the brain cannot have a higher O₂ concentration than the systemic arteries.

667 **Ca_i^{2+} prevented from becoming negative.**

668 The original model allowed the states that represented the neuronal Ca^{2+} levels to become numerically
669 negative if the effect of the corresponding neuron activity was negative enough. Negative enough
670 means that during stimulation the state of the neuronal activity N_i becomes so negative that its
671 contribution overtakes the corresponding $sinkCa_i^{2+}$ -term and the Ca_i^{2+} -state becomes negative. This
672 was addressed in the expanded model by introducing a softplus activation function in the equation for
673 the Ca_i^{2+} -states, to prevent the inflow term that corresponds to stimulation from the neuronal activity
674 N_i to be smaller than 0. Meaning that the inflow of Ca^{2+} will never go below the baseline. This means
675 that the differential equation for the Ca_i^{2+} states are formulated as:

$$\frac{d}{dt} Ca_i^{2+} = \ln(1 + \exp[k_{Ca} + k_{Ca,i} * N_i]) - sinkCa_i * Ca_i^{2+} \quad (5)$$

676

677 where Ca_i^{2+} is the collective level of Ca^{2+} for neuron type i ; k_{Ca} and $k_{Ca,i}$ are general and neuron-type-
678 specific scaling parameter respectively; N_i is the neuronal activity of neuron type i ; and $sinkCa_i^{2+}$ is a
679 collective term for the reduction in the Ca^{2+} levels.

680 **Changed CMRO₂ dependencies.**

681 In the original model, the calculation of the overall CMRO₂ depended on the activity of the different
682 neuron populations N_i . However, much like the Ca_i^{2+} states, this becomes a problem if N_i becomes
683 negative. Therefore, the expression for CMRO₂ was changed to be proportional to Ca_i^{2+} , rather than

684 N_i . Additionally, individual scaling parameters for the different neuron populations contributions to the
 685 total $CMRO_2$ were introduced. This resulted in the following expression for $CMRO_2$:

$$CMRO_2 = CMRO_{2,ss} * (1 + \sum_{\forall i} k_{CMRO_{2,i}} * Ca_i^{2+}) \quad (6)$$

686 Where $CMRO_2$ is the local region's overall metabolic rate of O_2 ; $CMRO_{2,ss}$ is the metabolic rate at
 687 baseline; $k_{CMRO_{2,i}}$ is the scaling parameter for the metabolic contribution of neuron population i ; and
 688 Ca_i^{2+} are the Ca^{2+} levels for neuron population i .

689 Reformulated intraneuronal signalling, introduced GABA and Glutamate State and a saturated 690 neuronal activity N_i

691 In the original model, the effects of neurotransmitters glutamate and GABA (i.e., inhibitory/excitatory
 692 pathways) are integrated in the states that represent the neuronal activity N_i . To make the model more
 693 readable and to better account for the excitatory and inhibitory regulation between, and within, the
 694 neuronal populations the expanded model introduces additional states for glutamate and GABA. The
 695 glutamate state increases the different neuronal activities N_i , while the GABA state decreases neuronal
 696 activities (Figure 8A). Additionally, a saturating effect was added to the neuronal activity induced by
 697 the experimental stimulations, meaning that for prolonged high-intensity stimulations, the increase in
 698 neuronal activity caused by the stimulation is capped to the value determined by the parameter
 699 estimation. All in all, these reformulations, and additions to the neuronal signalling mean that for the
 700 expanded model the equations for N_i states are formulated as:

$$\frac{d}{dt} N_i = k_{u,i} * u_i * \max(N_{max,i} - N_i, 0) + k_{PF,i} * Glutamate + k_{IN,i} * GABA - sink_{N_i} * N_i \quad (7)$$

701 where u_i is the stimulation function; $N_{max,i}$ is the parameter determining the saturation in the
 702 stimulating effect i.e., the stimulation term becomes 0 when $N_i > N_{max,i}$; *glutamate* and *GABA* are
 703 the changes in glutamate and GABA levels respectively; $k_{u,i}$, $k_{PF,i}$, $k_{IN,i}$, and $sink_{N_i}$ are scaling
 704 parameters scaling the effects of the stimulation, the neuronal activation caused by glutamate, the
 705 neuronal inhibition caused by GABA, and the general return to baseline neuronal activity, respectively.
 706 The levels of glutamate and GABA are implemented as

$$\frac{d}{dt} GABA = k_{GABA,NO} * Ca_{NO}^{2+} + k_{Glut,NPY} * Ca_{NPY}^{2+} + k_{Glut,Ast} * Ca_{Ast}^{2+} - sink_{Gaba} * GABA \quad (8)$$

$$\frac{d}{dt} Glutamate = k_{GABA,Pyr} * Ca_{Pyr}^{2+} + k_{GABA,Ast} * Ca_{Ast}^{2+} - sink_{Glut} * Glutamate \quad (9)$$

708 Where $k_{Glut,i}$ and $k_{GABA,i}$ are kinetic rate parameters determining the release of glutamate and GABA
 709 from the respective neuron populations; Ca_i^{2+} are the Ca^{2+} levels for the respective neuron
 710 populations; $sink_i$ is a parameter determining the rate at which the glutamate and GABA levels return
 711 to baseline.
 712

713 The stimulation function u_i is implemented as a repeating step function that alternates between 0 and
 714 1 depending on the stimulation scheme.

$$u_i(t) = \begin{cases} 1 & \text{for } t \in t_{on} \\ 0 & \text{otherwise} \end{cases} \quad (10)$$

715 where t_{on} is the set of time points determined by the stimulation pulse frequency, pulse width, and
716 total stimulation time. For example, a 4 second simulation at 1 Hz with a pulse width of 10 ms, t_{on} will
717 include the 10 first milliseconds of each second of the stimulation time.

718 **Addition of astrocytes as a regulating force for Glutamate and GABA levels**

719 In addition to the reformulation of the glutamate and GABA dynamics, the expanded model also has a
720 state representing the activity in astrocytes/glia cells. This state was introduced to allow the model a
721 higher degree of flexibility in regulating the levels of glutamate and GABA. The astrocyte activity is
722 formulated in the same way as equation 7. Although since there is no external stimulation of the
723 astrocytes the corresponding $k_{u,Ast} = 0$ i.e., the term representing the stimulation is removed.

724 **Model evaluation**

725 The model was evaluated with respect to its ability to describe experimental data taken from published
726 literature. This evaluation consisted of estimating the model parameters through iterative fitting to part
727 of the data, evaluating the model fit with statistical testing, analysing parameter identifiability and
728 model observability, and lastly validating model predictions against independent validation data not
729 used for model training.

730 **Parameter estimation**

731 The model's parameters were estimated by iteratively fitting the model to the training data. This was
732 achieved by using an optimization algorithm to minimize the sum of the squared residuals between the
733 model simulation and the experimental data. The squared residuals were, where applicable, weighted
734 by the Standard error of the mean (SEM) of the data. Thus, the function that was minimized was
735 formulated as:

$$f(\theta) = \sum_{\forall i} \sum_{\forall j} \left(\frac{\hat{y}_{i,j}(\theta) - \bar{y}_{i,j}}{SEM_{i,j}} \right)^2 \quad (11)$$

736

737 where $\hat{y}_{i,j}$ is the model simulated value of variable i at timepoint j ; θ are the model parameters; $\bar{y}_{i,j}$ is
738 the mean data point of variable i at timepoint j ; and $SEM_{i,j}$ is the standard error of the mean for
739 variable i at timepoint j . The function $f(\theta)$ was implemented as the objective function for a general
740 optimisation algorithm and minimised with respect to the parameters θ , such that:

$$\begin{aligned} \theta^* &= \arg \min_{\theta} f(\theta) \\ &s. t. lb \leq \theta \leq ub \end{aligned} \quad (12)$$

741

742 where θ^* are the optimal parameter values i.e., the parameter values that yield the best agreement
743 between the model and the data; and lb and ub are the lower and upper bounds of the parameter
744 estimation search space respectively.

745 Identifiability analysis

746 The identifiability of the model parameters was determined by applying a Markov Chain Monte Carlo
747 (MCMC) sampling. An adaptive multi-chain implementation of the Metropolis-Hastings algorithm,
748 using 10^6 samples, were used to generate a posterior distribution of parameter values. All parameter
749 sets θ that were deemed acceptable with respect to a χ^2 -test was saved and the practical parameter
750 identifiability for each parameter θ_i were determined by the confidence interval:

$$CI_{\alpha, DoF} = [f(\theta^*) \leq f(\theta) + \Delta_{\alpha}(\chi_{DoF}^2)] \quad (13)$$

751

752 where α is the significance level of the χ^2 -test; DoF is the number of degrees of freedom for the model;
753 $f(\theta^*)$ is the solution for the objective function in eq. 2 for the optimal parameters θ^* ; Δ_{α} is the α
754 quantile of the χ_{DoF}^2 statistic (Kreutz *et al.*, 2013; Maiwald *et al.*, 2016). For the analysis conducted in
755 this study, the DoF was set to the number of data points subtracted by the number of model
756 parameters. The estimated values for the optimal parameter values and the parameter confidence
757 intervals can be found in Supplementary Tables 2 and 3.

758 Model prediction of smaller pulse widths

759 In Figure 4, the model predictions of the 2 ms and 10 ms pulse width stimulation protocol, presented
760 by Vazquez *et al.* 2018 (Vazquez, Fukuda and Kim, 2018), are depicted. As the stimulation does not
761 linearly affect the system, or model, we allowed the parameters governing the stimulation effect,
762 k_{u1} , k_{u2} , and k_{u3} , to be scaled for these predictions. Note that no other parameters were altered, and
763 the scaling does not amount to re-training of the model. Rather, the scaling is considered a mechanism
764 for interpreting the effects of the stimulation. The scaling factor is described below.

$$k_{ui_pw} = \left(\frac{pw_{30}}{pw_j} + \frac{\max(HbT_{pw})}{\max(HbT_{30})} \right) * k_{ui_30} \quad (14)$$

765 Where, k_{ui_pw} are the rescaled parameters for the different pulse widths (pw), $i = \{1, 2, 3\}$ and $pw =$
766 $\{2, 10\}$, HbT_{pw} are the mean values of the HbT data for the different pulse widths, HbT_{30} is the mean
767 value for the HbT data corresponding to the 30 ms experiment, and k_{ui_30} are the estimated model
768 parameters, obtained from the model training.

769 Experimental data

770 The main computational analysis of the work presented here considered experimental data from three
771 previously published studies. The first of which was presented by Vazquez *et al.* in 2018, where they
772 investigated the contribution of different types of neurons to the hemodynamic response and the
773 metabolic load of the NVC (Vazquez, Fukuda and Kim, 2018). The second study, presented by Moon *et*
774 *al.* in 2021, further investigated the contributions of excitatory and inhibitory types of neurons to the
775 fMRI-BOLD response (Moon *et al.*, 2021). The third and final study was presented by Lee *et al.* in 2020
776 and investigated the hemodynamic response when selectively stimulating different subpopulations of
777 inhibitory interneurons (Lee *et al.*, 2020). All three of these studies used optogenetic mice to selectively
778 stimulate different types of neurons. That is the use of mice that have been genetically engineered to
779 express the light-sensitive Channelrhodopsin-2 (ChR2) ion channel in specific neuron populations
780 (Nagel *et al.*, 2003; Arenkiel *et al.*, 2007). The light-sensitive properties of ChR2 mean a light pulse can
781 be used to open the ion channel and thus selectively activate specific neuron populations (Fenno,
782 Yizhar and Deisseroth, 2011). All the data used in this work were sourced from figures published in
783 previous studies.

784 Data describing the neurovascular response for excitatory and inhibitory stimulation.

785 In their study from 2018, Vazquez *et al.* used OIS imaging to measure the relative levels of oxygenated
786 Hb (HbO), reduced or deoxygenated Hb (HbR), and the total amount of Hb (HbT) in the somatosensory
787 cortex of anesthetized mice. They also use laser doppler flowmetry (LDF) to measure CBF. In this study,
788 they consider data from 41 transgenic mice, 22 of which had inhibitory neurons expressing Chr2 via
789 the vesicular GABA transporter (VGAT)(Zhao and Zhang, 2011; Vazquez, Fukuda and Kim, 2018), and 19
790 had excitatory neurons expressing Chr2 via the thymus cell antigen 1 (Thy1) promoter (Vazquez *et al.*,
791 2014). The mice were exposed to optogenetic stimulation consisting of light pulses with an amplitude
792 of 1 mW, a frequency of 5 Hz, and pulse widths of 2 ms, 10 ms, and 30 ms were evaluated. The total
793 stimulation time for the optogenetic stimulation was 4 seconds. The authors also evaluated the
794 hemodynamic response to sensory forelimb (FL) stimulation by applying a 1.2 mA, 4Hz electric pulse
795 for 0.5 ms to one of the mice's forepaws. The mice were anesthetized using an initial dose of ketamine
796 (75 mg/kg) and xylazine (10 mg/kg), and a continuous supply of ketamine (30 mg/kg/h) during the
797 experiments. For further details please see the original publication (Vazquez, Fukuda and Kim, 2018).
798 The data considered in this present work mainly comes from the experiment entitled "*Experiment 5*"
799 in the original publication that investigates the differences in the hemodynamic responses and CMRO₂
800 invoked by optogenetic photo-stimulation of excitatory and inhibitory neurons.

801 Data illustrating the effects of stimulation intensity on the neurovascular response.

802 Building on the findings published by Vazquez *et al.* in 2018 (Vazquez, Fukuda and Kim, 2018), in their
803 study from 2021 Moon *et al.* investigate the contributions of excitatory and inhibitory neuronal activity
804 to the fMRI-BOLD response (Moon *et al.*, 2021). In this study, the authors measured the fMRI-BOLD
805 response for both excitatory, inhibitory, and sensory stimulation from the different regions of the brain
806 in optogenetic mice. OIS imaging was also used to quantify changes in the levels of HbO, HbR, and HbT
807 for inhibitory stimulation. This study used 17 VGAT-Chr2 mice for inhibitory stimulation, 6 mice that
808 expressed Chr2 via the calcium-calmodulin-dependent protein Kinase II (CaMKII) gene for excitatory
809 stimulation, and 5 wild-type non-transgenic C57BL/6 mice as a control group. For the fMRI-BOLD
810 measurement, the mice were ontogenetically stimulated with 200 ms and 10 ms light pulses at
811 frequencies of 1 Hz and 20 Hz respectively, for a total stimulation length of 20 s. For the sensory
812 stimulation, an electrical current of 0.5 mA at 4 Hz was applied to the left forelimb for 20 seconds. The
813 fMRI measurements were collected at a magnetic field strength of 15.2T, with a repetition time (TR) of
814 310 ms, an echo time (TE) of 3 ms, and a flip angle (FA) of 30°. For the OIS measurements the same
815 optogenetic stimulation as for the fMRI experiment were used i.e., 200 ms and 10 ms light pulses at 1
816 Hz and 20 Hz, respectively. For the OIS measurements two different stimulation times were used,
817 namely one longer 20 s stimulation and one shorter 5 s stimulation. In this study the mice were
818 anesthetized with an initial dose of ketamine (100 mg/kg) and xylazine (10 mg/kg), and a continuous
819 supply of 25 mg/kg ketamine and 1.25 mg/kg xylazine during the experiments. For further details
820 please see the original publication (Moon *et al.*, 2021).

821 Data describing contributions to neurovascular response from different inhibitory interneuron
822 populations.

823 In their study published in 2020, Lee *et al.* investigate the differences in the NVC's hemodynamic
824 response if different subpopulations of GABAergic interneurons are stimulated. In this study, the
825 hemodynamic responses in mice for stimulating NO-interneurons and SOM-interneurons were
826 compared with each other, and with a sensory whisker stimulation. OIS imaging where used to measure
827 the relative changes in the levels of HbT, HbO, and HbR. The study cohort consisted of a total of 39

828 mice, male and female. 18 of these mice were nNOS-CreER × Chr2-EYFP (nNOS-ChR2) mice, selectively
829 expressing Chr2 in NO-interneurons. 12 mice were Sstm2.1Crezjh/j × Chr2-EYFP (SST-ChR2) mice,
830 selectively expressing Chr2 in NO-interneurons and SST interneurons. Lastly, 5 non-transgenic
831 C57BL/6J mice and 4 non-ChR2 expressing nNOS-ChR2 mice were used for sensory stimulation. The
832 optogenetic stimulation paradigms consisted of 10 ms light pulses at 20 Hz applied to the subjects for
833 shorter 2 s and longer 16 s stimulation periods, respectively. For the sensory stimulations, the whiskers
834 were deflected at 5 Hz for either 2 or 16 s. The animals were anesthetized with an initial injection of
835 fentanyl-fluanisone and midazolam diluted in water (7 ml/kg), and a continuous supply of isoflurane in
836 oxygen at 0.8 L/min during the experiments. Please see the original publication for further details (Lee
837 *et al.*, 2020).

838 [Model Implementation](#)

839 The mathematical model described in the “Model structure” section above was implemented and
840 simulated using the MATLAB version of the “Advanced Multi-language Interface to CVODEs and IDAs”
841 (AMICI) toolbox (Fröhlich *et al.*, 2021). The parameter estimation and model evaluation were done
842 using the “Metaheuristics for Systems Biology and Bioinformatics Global Optimization” (MEIGO)
843 toolbox for MATLAB (Egea *et al.*, 2014). Within the MEIGO framework, the enhanced scatter search
844 (eSS) global algorithm and the dynamic hill climbing (dhc) local algorithm were used to solve the
845 optimization problem formulated in the section “Model Evaluation”. For the identifiability analysis, the
846 MATLAB implementation of the “Parameter ESTimation TOolbox” (PESTO) (Stapor *et al.*, 2018) was used
847 for the MCMC sampling. This implementation used a parallel tempering algorithm (Ballnus *et al.*, 2018)
848 to generate the posterior parameter distributions. The area under the curve calculations presented
849 here were calculated using a numerical integration via a trapezoidal method. All the computational
850 implementations of the model and analyses described above were done in MATLAB by MathWorks Inc.
851 releases R2017b and R2021b. All model implementation and files required to reproduce the work
852 presented herein can be found at: <https://github.com/Podde1/MetaAnalysisNVCInhibitoryNeurons.git>
853 and a permanent copy available at Zenodo (DOI: [10.5281/zenodo.13747286](https://doi.org/10.5281/zenodo.13747286)).

854

855 [Acknowledgements](#)

856 The computational resources required for these analyses were provided by the National
857 Supercomputer Centre (NSC), funded by Linköping University.

858

859 [Funding information](#)

860 GC acknowledges support from the Swedish Research Council (2018-05418, 2018-03319), CENIIT
861 (15.09), the Swedish Foundation for Strategic Research (ITM17-0245), SciLifeLab National COVID-19
862 Research Program financed by the Knut and Alice Wallenberg Foundation (2020.0182), the H2020
863 project PRECISE4Q (777107), the Swedish Fund for Research without Animal Experiments (F2019-
864 0010), ELLIIT (2020-A12), VINNOVA (VisualSweden, 2020-04711), and the Horizon Europe project
865 STRATIF-AI (101080875). GC acknowledges scientific support from the Exploring Inflammation in
866 Health and Disease (X-HiDE) Consortium, which is a strategic research profile at Örebro University
867 funded by the Knowledge Foundation (20200017). ME acknowledges support from the Swedish
868 Research Council (2022-02886). SDB acknowledges support from NIH U24EB028998, NYS SCIRB
869 DOH01-C38328GG and NIMH P50MH109429.

870 **Author Contributions**

871 **Conceptualization:** NS, HP, SS, ME, SDB, and GC. **Formal model analysis:** NS and HP. **Data curation:** NS
872 and HP. **Visualization:** NS and HP. **Supervision:** GC, SS, ME, and SDB. **Funding acquisition:** GC, ME, and
873 SDB.

874 All authors were involved in writing and reviewing the manuscript. All authors read and approved the
875 final manuscript.

876

877 References

- 878 Arenkiel, B.R. *et al.* (2007) 'In Vivo Light-Induced Activation of Neural Circuitry in Transgenic Mice
879 Expressing Channelrhodopsin-2', *Neuron*, 54(2), pp. 205–218. Available at:
880 <https://doi.org/10.1016/j.neuron.2007.03.005>.
- 881 Ballnus, B. *et al.* (2018) 'Bayesian parameter estimation for biochemical reaction networks using
882 region-based adaptive parallel tempering', *Bioinformatics*, 34(13), pp. i494–i501. Available at:
883 <https://doi.org/10.1093/bioinformatics/bty229>.
- 884 Barrett, M.J.P. and Suresh, V. (2015) 'Improving estimates of the cerebral metabolic rate of oxygen
885 from optical imaging data', *NeuroImage*, 106, pp. 101–110. Available at:
886 <https://doi.org/10.1016/j.neuroimage.2014.11.041>.
- 887 Dadarlat, M.C., Sun, Y.J. and Stryker, M.P. (2024) 'Activity-dependent recruitment of inhibition and
888 excitation in the awake mammalian cortex during electrical stimulation', *Neuron*, 112(5), pp. 821-
889 834.e4. Available at: <https://doi.org/10.1016/j.neuron.2023.11.022>.
- 890 Desjardins, M. *et al.* (2019) 'Awake Mouse Imaging: From Two-Photon Microscopy to Blood Oxygen
891 Level-Dependent Functional Magnetic Resonance Imaging', *Biological Psychiatry: Cognitive
892 Neuroscience and Neuroimaging*, 4(6), pp. 533–542. Available at:
893 <https://doi.org/10.1016/j.bpsc.2018.12.002>.
- 894 Di Volo, M. *et al.* (2019) 'Biologically Realistic Mean-Field Models of Conductance-Based Networks of
895 Spiking Neurons with Adaptation', *Neural Computation*, 31(4), pp. 653–680. Available at:
896 https://doi.org/10.1162/neco_a_01173.
- 897 Drew, P.J., Shih, A.Y. and Kleinfeld, D. (2011) 'Fluctuating and sensory-induced vasodynamics in rodent
898 cortex extend arteriole capacity', *Proceedings of the National Academy of Sciences*, 108(20), pp.
899 8473–8478. Available at: <https://doi.org/10.1073/pnas.1100428108>.
- 900 Dura-Bernal, S. *et al.* (2019) 'NetPyNE, a tool for data-driven multiscale modeling of brain circuits',
901 *eLife*. Edited by U.S. Bhalla *et al.*, 8, p. e44494. Available at: <https://doi.org/10.7554/eLife.44494>.
- 902 Dura-Bernal, S., Griffith, E.Y., *et al.* (2023) 'Data-driven multiscale model of macaque auditory
903 thalamocortical circuits reproduces in vivo dynamics', *Cell Reports*, 42(11), p. 113378. Available at:
904 <https://doi.org/10.1016/j.celrep.2023.113378>.
- 905 Dura-Bernal, S., Neymotin, S.A., *et al.* (2023) 'Multiscale model of primary motor cortex circuits
906 predicts in vivo cell-type-specific, behavioral state-dependent dynamics', *Cell Reports*, 42(6), p.
907 112574. Available at: <https://doi.org/10.1016/j.celrep.2023.112574>.
- 908 Echagarruga, C.T. *et al.* (2020) 'nNOS-expressing interneurons control basal and behaviorally evoked
909 arterial dilation in somatosensory cortex of mice', *eLife*. Edited by A. Mishra *et al.*, 9, p. e60533.
910 Available at: <https://doi.org/10.7554/eLife.60533>.
- 911 Egea, J.A. *et al.* (2014) 'MEIGO: an open-source software suite based on metaheuristics for global
912 optimization in systems biology and bioinformatics', *BMC Bioinformatics*, 15(1), p. 136. Available at:
913 <https://doi.org/10.1186/1471-2105-15-136>.
- 914 Fenno, L., Yizhar, O. and Deisseroth, K. (2011) 'The Development and Application of Optogenetics',
915 *Annual Review of Neuroscience*, 34(1), pp. 389–412. Available at: <https://doi.org/10.1146/annurev-neuro-061010-113817>.

- 917 Fröhlich, F. *et al.* (2021) 'AMICI: High-Performance Sensitivity Analysis for Large Ordinary Differential
918 Equation Models', *Bioinformatics* [Preprint], (bt227). Available at:
919 <https://doi.org/10.1093/bioinformatics/btab227>.
- 920 Gore, J.C. (2003) 'Principles and practice of functional MRI of the human brain', *Journal of Clinical*
921 *Investigation*, 112(1), pp. 4–9. Available at: <https://doi.org/10.1172/JCI200319010>.
- 922 Griffeth, V.E. and Buxton, R.B. (2011) 'A theoretical framework for estimating cerebral oxygen
923 metabolism changes using the calibrated-BOLD method: modeling the effects of blood volume
924 distribution, hematocrit, oxygen extraction fraction, and tissue signal properties on the BOLD signal',
925 *NeuroImage*, 58(1), pp. 198–212. Available at: <https://doi.org/10.1016/j.neuroimage.2011.05.077>.
- 926 Harris, K.D. and Shepherd, G.M.G. (2015) 'The neocortical circuit: themes and variations', *Nature*
927 *Neuroscience*, 18(2), pp. 170–181. Available at: <https://doi.org/10.1038/nn.3917>.
- 928 Havlicek, M. *et al.* (2015) 'Physiologically informed dynamic causal modeling of fMRI data',
929 *NeuroImage*, 122, pp. 355–372. Available at: <https://doi.org/10.1016/j.neuroimage.2015.07.078>.
- 930 Hillman, E.M.C. (2014) 'Coupling mechanism and significance of the BOLD signal: a status report',
931 *Annual Review of Neuroscience*, 37, pp. 161–181. Available at: <https://doi.org/10.1146/annurev-neuro-071013-014111>.
- 932 Kim, J.H. and Ress, D. (2016) 'Arterial impulse model for the BOLD response to brief neural activation',
933 *NeuroImage*, 124(0 0), pp. 394–408. Available at: <https://doi.org/10.1016/j.neuroimage.2015.08.068>.
- 934
- 935 Kim, S.-G. and Ogawa, S. (2012) 'Biophysical and physiological origins of blood oxygenation level-
936 dependent fMRI signals', *Journal of Cerebral Blood Flow & Metabolism*, 32(7), pp. 1188–1206.
937 Available at: <https://doi.org/10.1038/jcbfm.2012.23>.
- 938 Krawchuk, M.B. *et al.* (2020) 'Optogenetic assessment of VIP, PV, SOM and NOS inhibitory neuron
939 activity and cerebral blood flow regulation in mouse somato-sensory cortex', *Journal of Cerebral*
940 *Blood Flow & Metabolism*, 40(7), pp. 1427–1440. Available at:
941 <https://doi.org/10.1177/0271678X19870105>.
- 942 Kreutz, C. *et al.* (2013) 'Profile likelihood in systems biology', *The FEBS Journal*, 280(11), pp. 2564–
943 2571. Available at: <https://doi.org/10.1111/febs.12276>.
- 944 Krogsgaard, A. *et al.* (2023) 'PV interneurons evoke astrocytic Ca²⁺ responses in awake mice, which
945 contributes to neurovascular coupling', *Glia*, 71(8), pp. 1830–1846. Available at:
946 <https://doi.org/10.1002/glia.24370>.
- 947 Lee, H. *et al.* (2021) 'Differential effect of anesthesia on visual cortex neurons with diverse population
948 coupling', *Neuroscience*, 458, pp. 108–119. Available at:
949 <https://doi.org/10.1016/j.neuroscience.2020.11.043>.
- 950 Lee, H., Wang, S. and Hudetz, A.G. (2020) 'State-Dependent Cortical Unit Activity Reflects Dynamic
951 Brain State Transitions in Anesthesia', *The Journal of Neuroscience*, 40(49), pp. 9440–9454. Available
952 at: <https://doi.org/10.1523/JNEUROSCI.0601-20.2020>.
- 953 Lee, J. *et al.* (2021) 'Opposed hemodynamic responses following increased excitation and
954 parvalbumin-based inhibition', *Journal of Cerebral Blood Flow & Metabolism*, 41(4), pp. 841–856.
955 Available at: <https://doi.org/10.1177/0271678X20930831>.

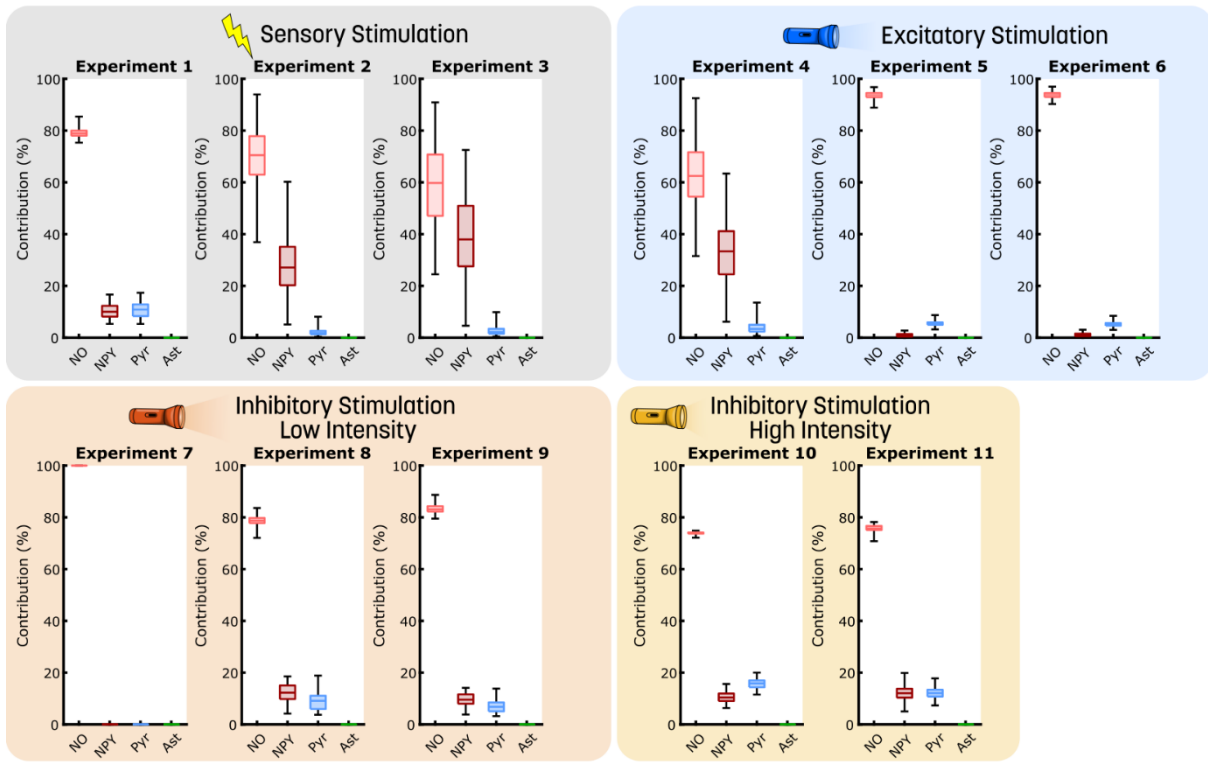
- 956 Lee, L. *et al.* (2020) 'Key Aspects of Neurovascular Control Mediated by Specific Populations of
957 Inhibitory Cortical Interneurons', *Cerebral Cortex*, 30(4), pp. 2452–2464. Available at:
958 <https://doi.org/10.1093/cercor/bhz251>.
- 959 Logothetis, N.K. *et al.* (2001) 'Neurophysiological investigation of the basis of the fMRI signal', *Nature*,
960 412(6843), pp. 150–157. Available at: <https://doi.org/10.1038/35084005>.
- 961 Logothetis, N.K. (2003) 'The Underpinnings of the BOLD Functional Magnetic Resonance Imaging
962 Signal', *The Journal of Neuroscience*, 23(10), pp. 3963–3971. Available at:
963 <https://doi.org/10.1523/JNEUROSCI.23-10-03963.2003>.
- 964 Logothetis, N.K. (2008) 'What we can do and what we cannot do with fMRI', *Nature*, 453(7197), pp.
965 869–878. Available at: <https://doi.org/10.1038/nature06976>.
- 966 Lundengård, K. *et al.* (2016) 'Mechanistic Mathematical Modeling Tests Hypotheses of the
967 Neurovascular Coupling in fMRI.', *PLoS computational biology*, 12(6), p. e1004971. Available at:
968 <https://doi.org/10.1371/journal.pcbi.1004971>.
- 969 Maiwald, T. *et al.* (2016) 'Driving the Model to Its Limit: Profile Likelihood Based Model Reduction',
970 *PLOS ONE*, 11(9), p. e0162366. Available at: <https://doi.org/10.1371/journal.pone.0162366>.
- 971 Meyer, H.S. *et al.* (2011) 'Inhibitory interneurons in a cortical column form hot zones of inhibition in
972 layers 2 and 5A', *Proceedings of the National Academy of Sciences of the United States of America*,
973 108(40), pp. 16807–16812. Available at: <https://doi.org/10.1073/pnas.1113648108>.
- 974 Moon, H.S. *et al.* (2021) 'Contribution of Excitatory and Inhibitory Neuronal Activity to BOLD fMRI',
975 *Cerebral Cortex*, 31(9), pp. 4053–4067. Available at: <https://doi.org/10.1093/cercor/bhab068>.
- 976 Nagel, G. *et al.* (2003) 'Channelrhodopsin-2, a directly light-gated cation-selective membrane
977 channel', *Proceedings of the National Academy of Sciences*, 100(24), pp. 13940–13945. Available at:
978 <https://doi.org/10.1073/pnas.1936192100>.
- 979 Ogawa, S. *et al.* (1990) 'Brain magnetic resonance imaging with contrast dependent on blood
980 oxygenation', *Proceedings of the National Academy of Sciences of the United States of America*,
981 87(24), pp. 9868–9872. Available at: <https://doi.org/10.1073/pnas.87.24.9868>.
- 982 Rosenbaum, R., Rubin, J. and Doiron, B. (2012) 'Short Term Synaptic Depression Imposes a Frequency
983 Dependent Filter on Synaptic Information Transfer', *PLOS Computational Biology*, 8(6), p. e1002557.
984 Available at: <https://doi.org/10.1371/journal.pcbi.1002557>.
- 985 Stapor, P. *et al.* (2018) 'PESTO: Parameter ESTimation TOolbox', *Bioinformatics*, 34(4), pp. 705–707.
986 Available at: <https://doi.org/10.1093/bioinformatics/btx676>.
- 987 Sten, S. *et al.* (2020) 'A quantitative analysis of cell-specific contributions and the role of anesthetics
988 to the neurovascular coupling', *NeuroImage*, 215, p. 116827. Available at:
989 <https://doi.org/10.1016/j.neuroimage.2020.116827>.
- 990 Sten, S. *et al.* (2023) 'A quantitative model for human neurovascular coupling with translated
991 mechanisms from animals', *PLOS Computational Biology*, 19(1), p. e1010818. Available at:
992 <https://doi.org/10.1371/journal.pcbi.1010818>.

- 993 Tesler, F., Linne, M.-L. and Destexhe, A. (2023) 'Modeling the relationship between neuronal activity
994 and the BOLD signal: contributions from astrocyte calcium dynamics', *Scientific Reports*, 13(1), p.
995 6451. Available at: <https://doi.org/10.1038/s41598-023-32618-0>.
- 996 Tsodyks, M.V. and Markram, H. (1997) 'The neural code between neocortical pyramidal neurons
997 depends on neurotransmitter release probability', *Proceedings of the National Academy of Sciences*,
998 94(2), pp. 719–723. Available at: <https://doi.org/10.1073/pnas.94.2.719>.
- 999 Uhlirova, H. *et al.* (2016) 'Cell type specificity of neurovascular coupling in cerebral cortex', *eLife*.
1000 Edited by S.B. Nelson, 5, p. e14315. Available at: <https://doi.org/10.7554/eLife.14315>.
- 1001 Vazquez, A.L. *et al.* (2014) 'Neural and Hemodynamic Responses Elicited by Forelimb- and Photo-
1002 stimulation in Channelrhodopsin-2 Mice: Insights into the Hemodynamic Point Spread Function',
1003 *Cerebral Cortex (New York, NY)*, 24(11), pp. 2908–2919. Available at:
1004 <https://doi.org/10.1093/cercor/bht147>.
- 1005 Vazquez, A.L., Fukuda, M. and Kim, S.-G. (2018) 'Inhibitory Neuron Activity Contributions to
1006 Hemodynamic Responses and Metabolic Load Examined Using an Inhibitory Optogenetic Mouse
1007 Model', *Cerebral Cortex*, 28(11), pp. 4105–4119. Available at: <https://doi.org/10.1093/cercor/bhy225>.
- 1008 Yao, Z. *et al.* (2023) 'A high-resolution transcriptomic and spatial atlas of cell types in the whole
1009 mouse brain', *Nature*, 624(7991), pp. 317–332. Available at: <https://doi.org/10.1038/s41586-023-06812-z>.
- 1011 Zhang, W. *et al.* (2016) 'SYNAPTIC DEPRESSION IN DEEP NEURAL NETWORKS FOR SPEECH
1012 PROCESSING', *Proceedings of the ... IEEE International Conference on Acoustics, Speech, and Signal
1013 Processing. ICASSP (Conference)*, 2016, pp. 5865–5869. Available at:
1014 <https://doi.org/10.1109/ICASSP.2016.7472802>.
- 1015 Zhao, C.Y. and Zhang, G.H. (2011) 'Review on microencapsulated phase change materials (MEPCMs):
1016 Fabrication, characterization and applications', *Renewable and Sustainable Energy Reviews*, 15, pp.
1017 3813–3832. Available at: <https://doi.org/10.1016/j.rser.2011.07.019>.
- 1018

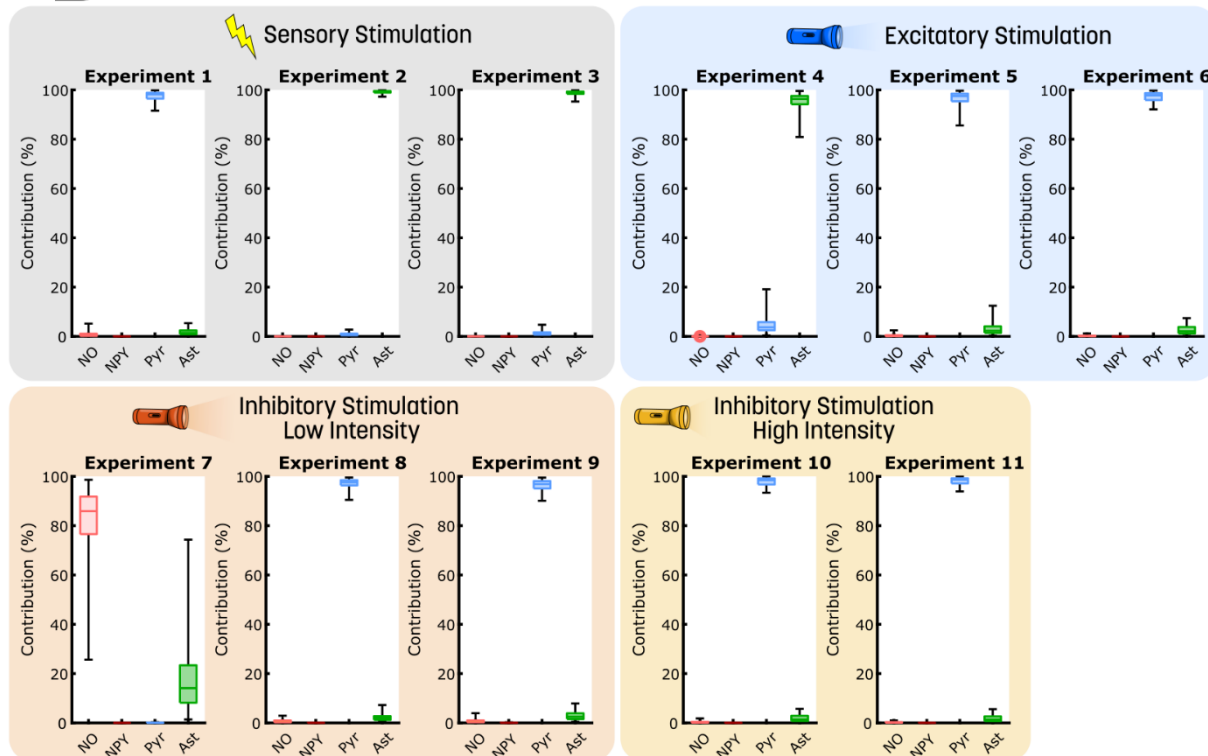
1019 Supplementary Figures

A Relative Contribution to CBV Signal

■ NO Interneurons ■ NPY Interneurons ■ Pyramidal Neurons ■ Astrocytes



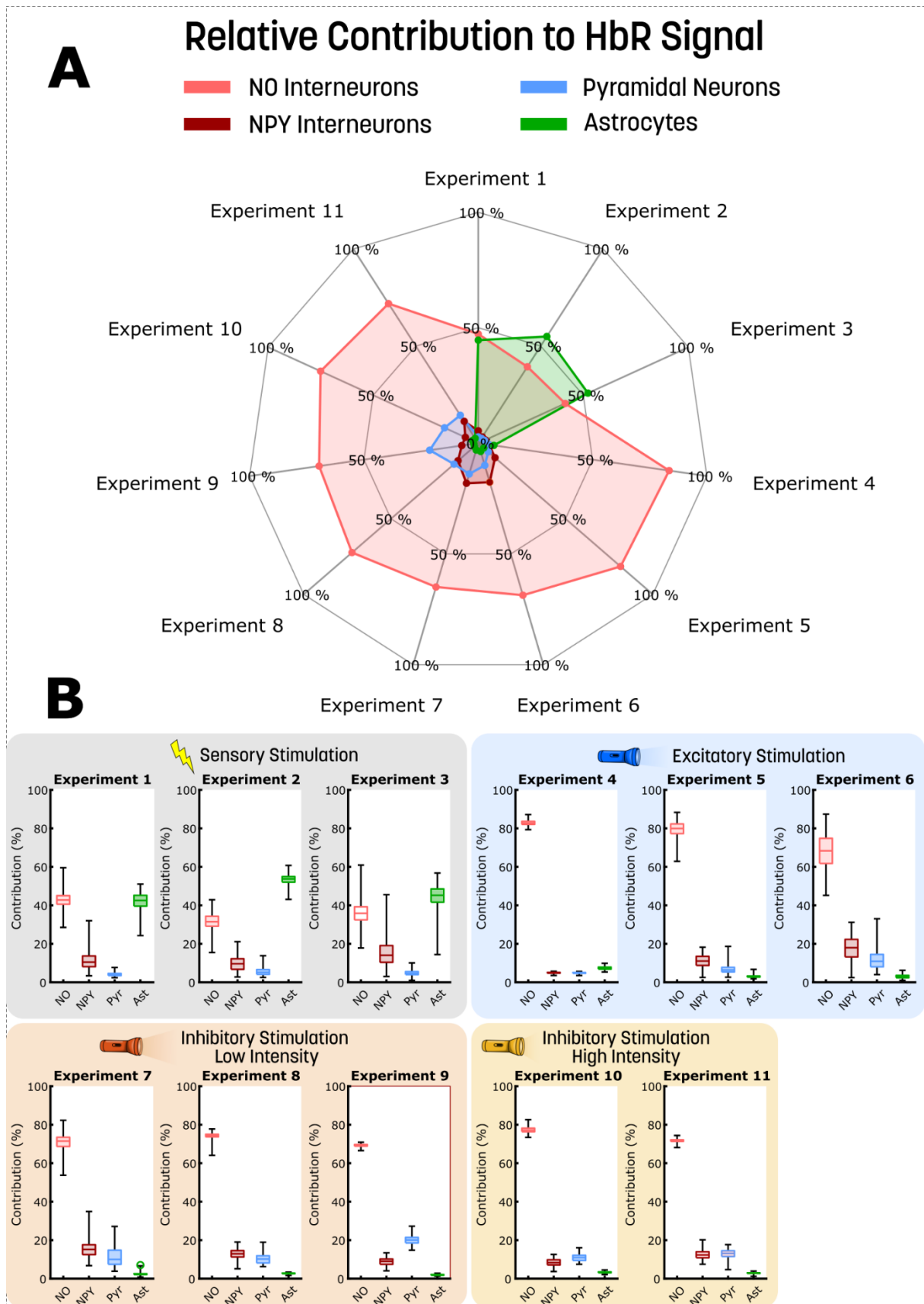
B Relative Contribution to CMRO₂ Signal



1020

1021 **Figure S1: The contribution of different neuronal populations to the CBV and CMRO₂ signal.** The contribution of
 1022 four different neuronal populations, nitric oxide (NO) interneurons (light red), neuropeptide Y (NPY) interneurons

1023 *(crimson), pyramidal neurons (Pyr, blue), and glia cells (Ast, green), are presented for 11 different experiments to*
1024 ***A**) cerebral vascular volume (CBV) and **B**) cerebral metabolic rate of oxygen (CMRO₂). The contributions are*
1025 *presented as boxplots, detailing the contribution of the four neuronal populations with uncertainty. The*
1026 *background of each experiment indicates the type of stimulation that generated these behaviours: grey is a*
1027 *sensory stimulation, blue is an optogenetic excitatory stimulation, orange is an optogenetic inhibitory low-*
1028 *intensity stimulation, and yellow is an optogenetic inhibitory high-intensity stimulation.*



1029

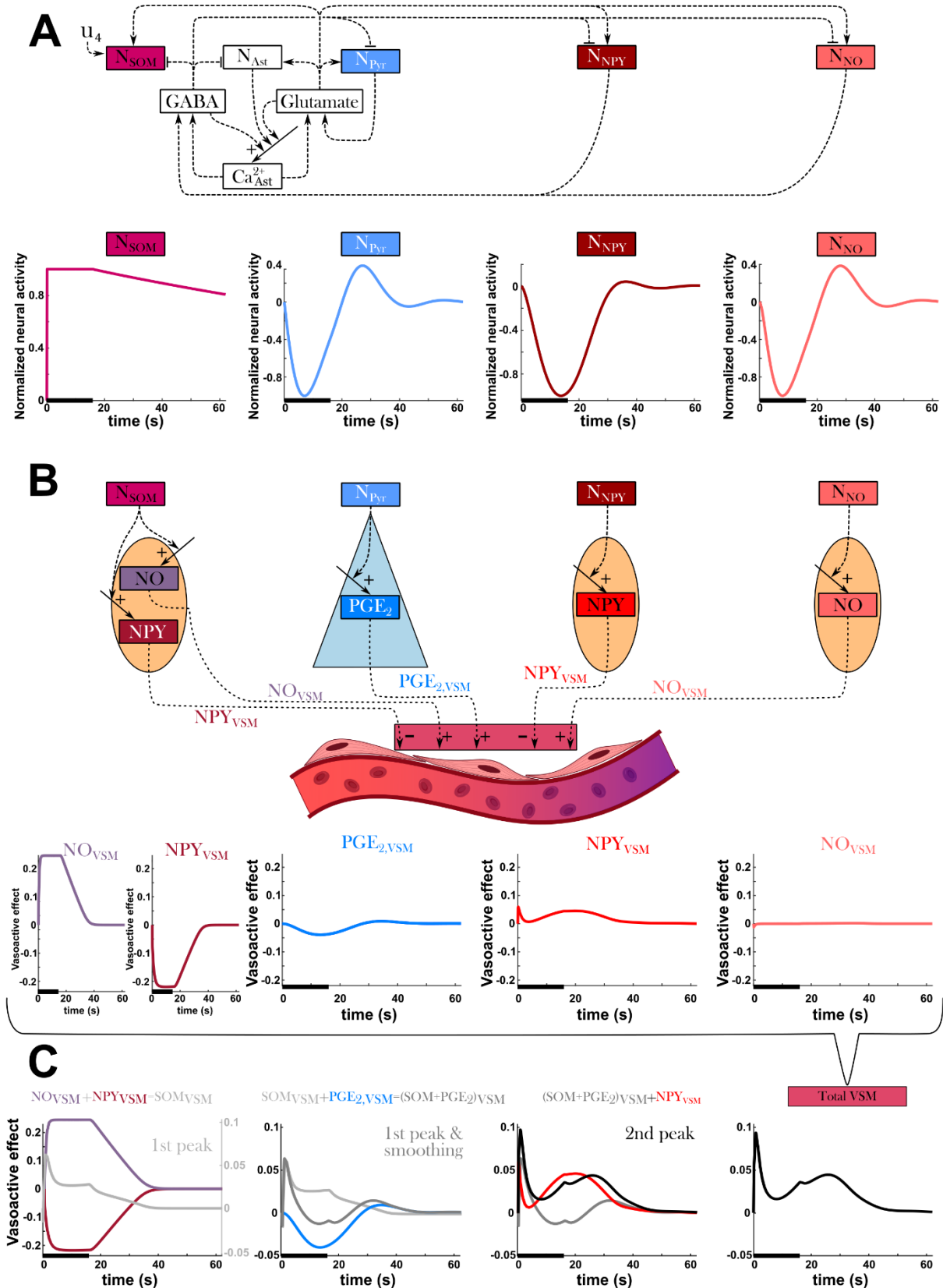
1030

1031

1032

Figure S2: The contribution of different neuronal populations to the HbR signal. A) The contribution of four different neuronal populations, nitric oxide (NO) interneurons (beige), neuropeptide Y (NPY) interneurons (red), pyramidal neurons (Pyr, light blue), and glia cells (Ast, green), to the deoxygenated haemoglobin (HbR) are

1033 *presented for 11 different experiments. B) Boxplots detailing the contribution of the four neuronal populations*
1034 *(NO beige, NPY red, Pyr light blue, Ast green), with uncertainty, for the 11 experiments presented in A. The*
1035 *background of each experiment indicates the type of stimulation that generated these behaviours: grey is a*
1036 *sensory stimulation, blue is an optogenetic excitatory stimulation, orange is an optogenetic inhibitory low-*
1037 *intensity stimulation, and yellow is an optogenetic inhibitory high-intensity stimulation.*



1038

1039

1040

1041

Figure S3: The delayed dilation of somatostatin-releasing interneurons is caused by different neuronal recovery speeds post-stimulation. A) A simplified overview of neural activity part of the model, including the extension of the somatostatin-releasing interneurons (SOM), for a 16 s long stimulation, u_4 , applied to the SOM

1042 *neurons. As the SOM neurons (ruby) are stimulated, GABA is produced which inhibits the other neurons which*
1043 *are not externally stimulated. This is further highlighted by the plots of the normalized neural activity for SOM*
1044 *(ruby), pyramidal (blue), NPY expressing (crimson), and NO expressing (light red) neurons. For these plots, the x-*
1045 *axis represents time in seconds. B) A simplified model overview of how the neural activity propagates to the*
1046 *vasoactive signalling substances. NO and PGE₂ dilate the vasculature, while NPY contracts. For the same 16 s*
1047 *long stimulation the vasoactive effect of NO (purple) and NPY (dark red), released by SOM neurons, PGE₂ (blue),*
1048 *released by pyramidal neurons, NPY (red), released by NPY interneurons, and NO (light red), released by NO*
1049 *interneurons, are shown. C) By sequentially adding the individual vasoactive effects together, we can identify the*
1050 *contribution of the different substances. NO and NPY released by the SOM neurons produces the initial peak and*
1051 *a plateau that returns to the baseline (grey line). Adding PGE₂ to the grey line transforms the plateau to the*
1052 *initial part of the second peak (dark grey line). Adding NPY released from the NPY interneurons further*
1053 *accentuates the initial peak and raises the amplitude of the second peak. NO released from the NO interneurons*
1054 *exhibit a weak impact on the total vasoactive response.*

1055 [Supplementary Table Legends](#)

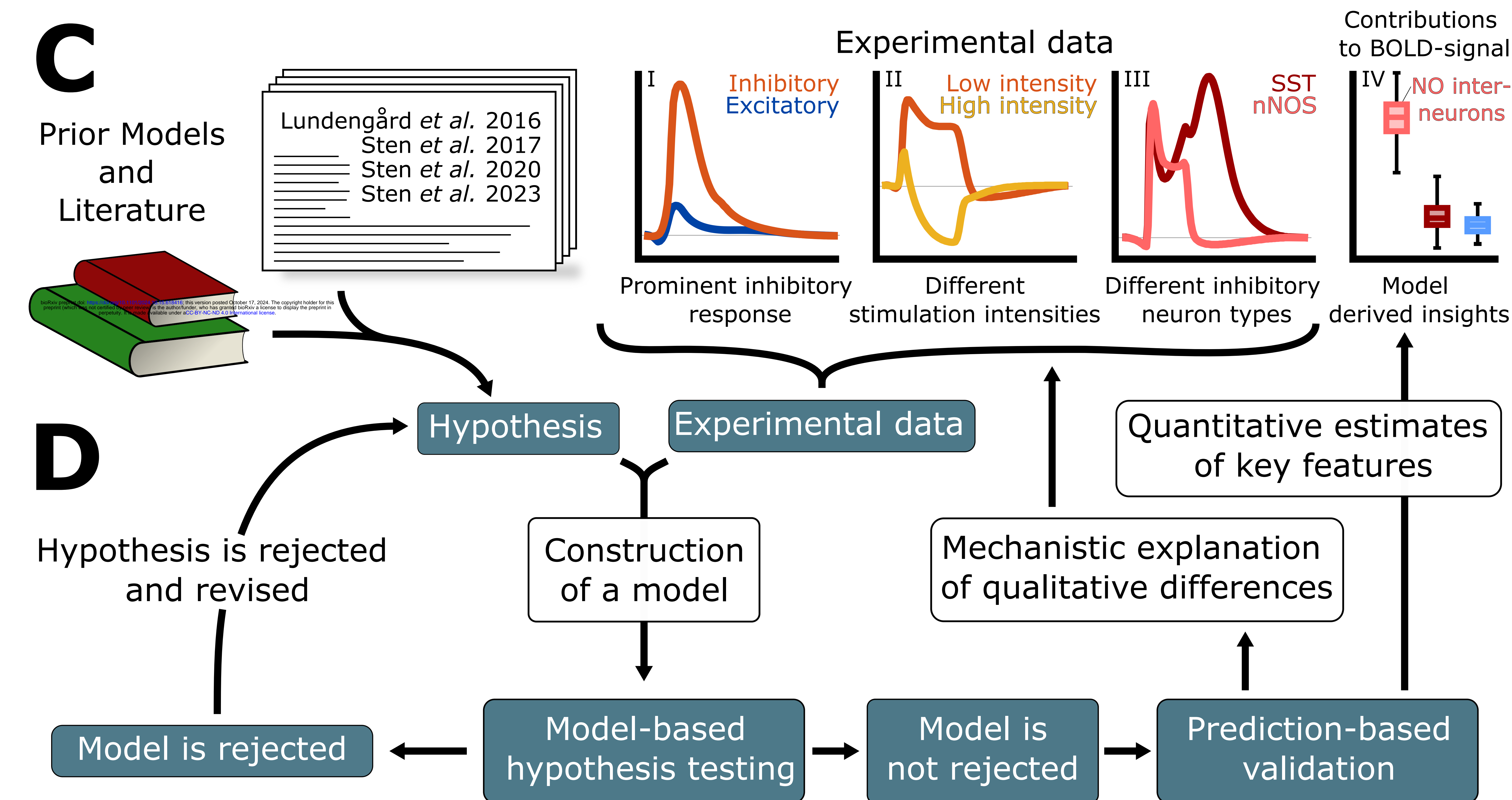
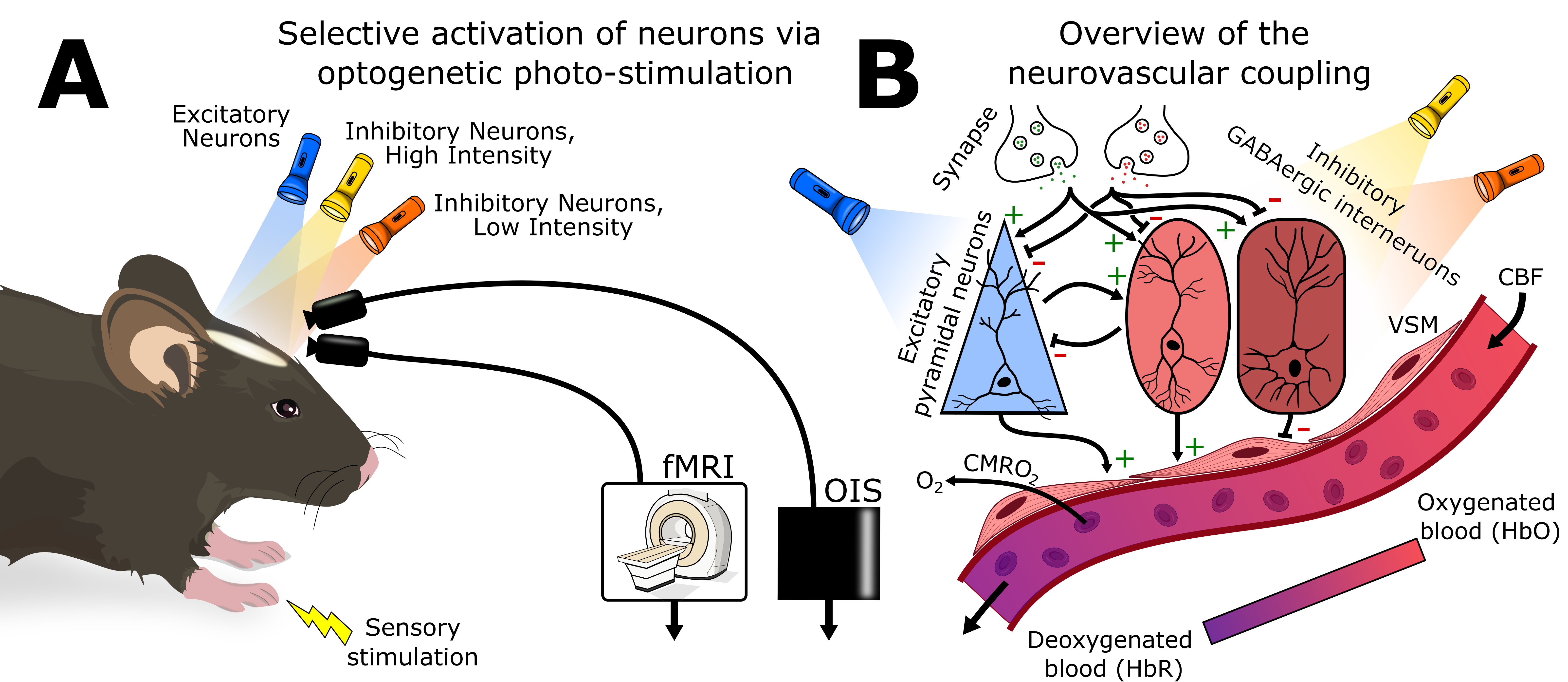
1056 **Table S1: Overview of the experimental protocol parameters.** The experimental stimulation protocol
1057 parameters are detailed for the 17 experiments analysed. The table includes the study of origin,
1058 stimulation type, stimulation duration, stimulation frequency, stimulation pulse duration in
1059 milliseconds and seconds, light exposure, stimulation strength or effect, the type of mouse and the
1060 utilized mouse strain, and the dosing of the anaesthesia agents. The colours indicate the stimulation
1061 type, where: grey is sensory stimulation, light blue is optogenetic excitatory stimulation, orange is
1062 optogenetic inhibitory low-intensity stimulation, yellow is optogenetic inhibitory high-intensity
1063 stimulation, and red is optogenetic somasomatic stimulation.

1064

1065 **Table S2: Model parameter values:** The model parameters are detailed in this table in log₁₀ scale. The
1066 columns detail: the parameter name, the best estimated value found during parameter estimation, the
1067 lower bound used during parameter estimation, the upper bound used during parameter estimation,
1068 the lowest value found for the confidence interval, and the highest value found for the confidence
1069 interval. Repeated parameters are named with an abbreviation to indicate which study and experiment
1070 they belong to.

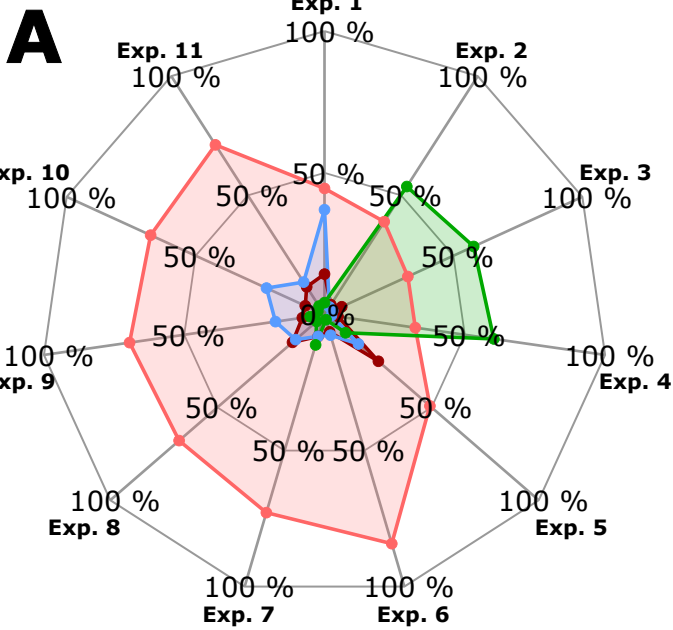
1071

1072 **Table S3: SOM model parameter values:** The model parameters are detailed in this table in log₁₀ scale.
1073 The columns detail: the parameter name, the best estimated value found during parameter estimation,
1074 the lower bound used during parameter estimation, the upper bound used during parameter
1075 estimation, the lowest value found for the confidence interval, and the highest value found for the
1076 confidence interval. Repeated parameters are named with an abbreviation to indicate which
1077 experiment they belong to.

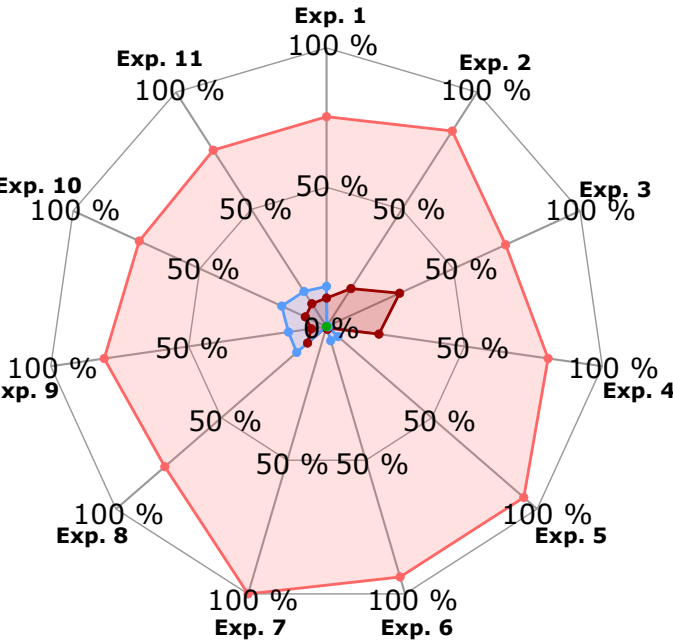


Relative Contribution to BOLD Signal

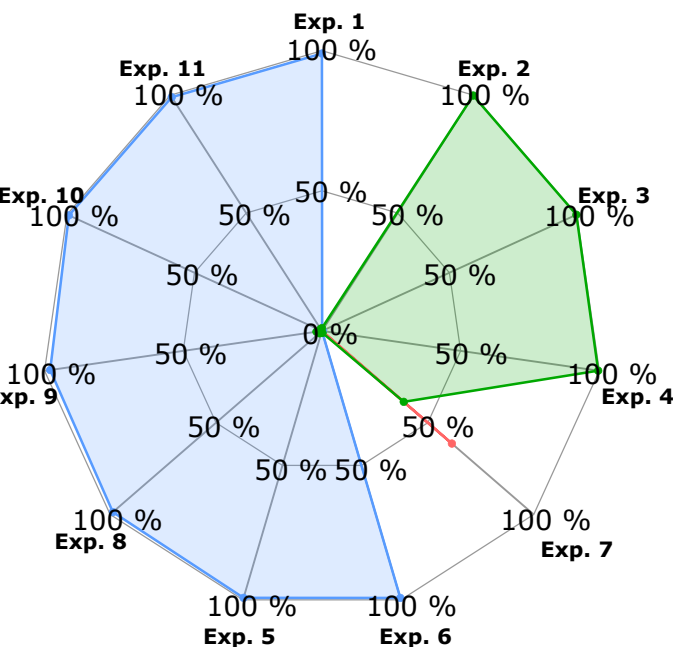
NO Interneurons NPY Interneurons Pyramidal Neurons Astrocytes



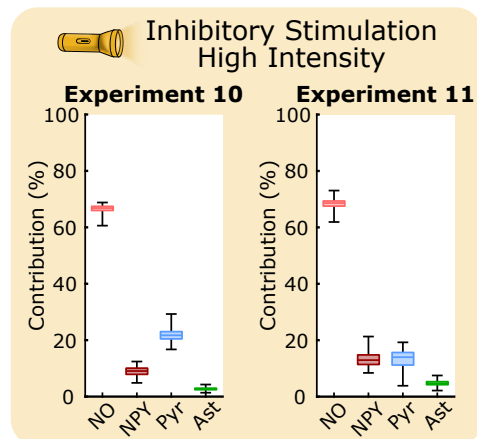
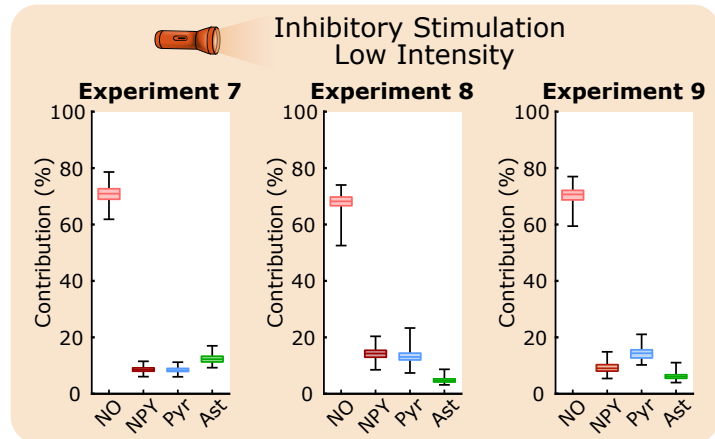
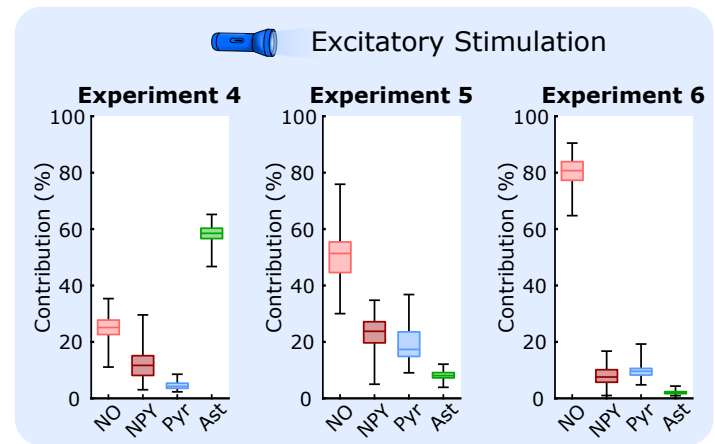
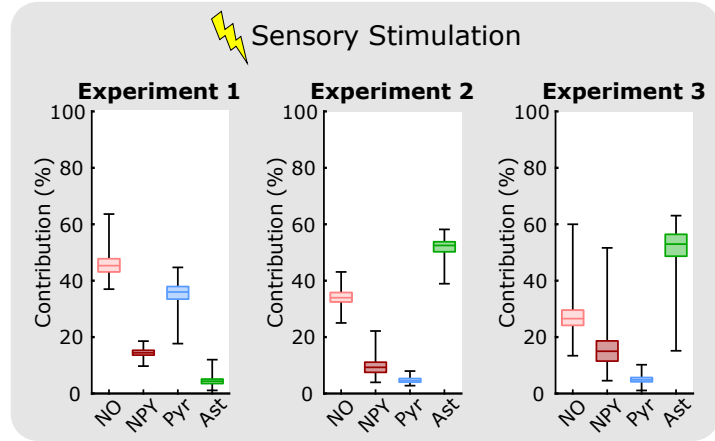
B Relative Contribution to CBV

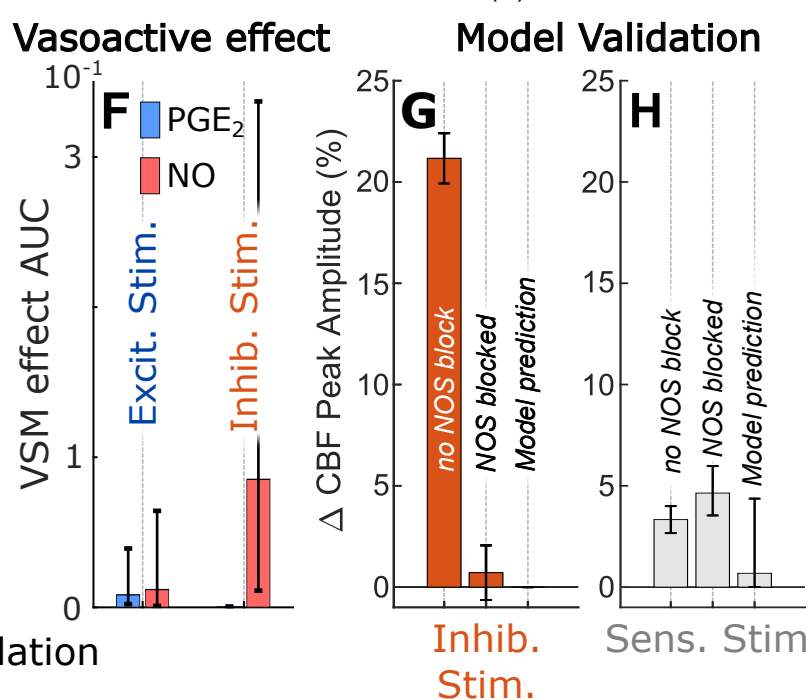
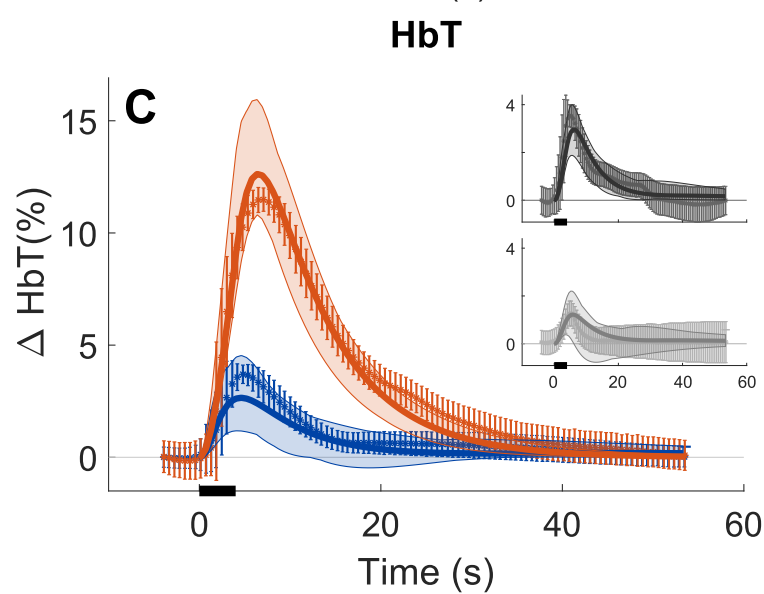
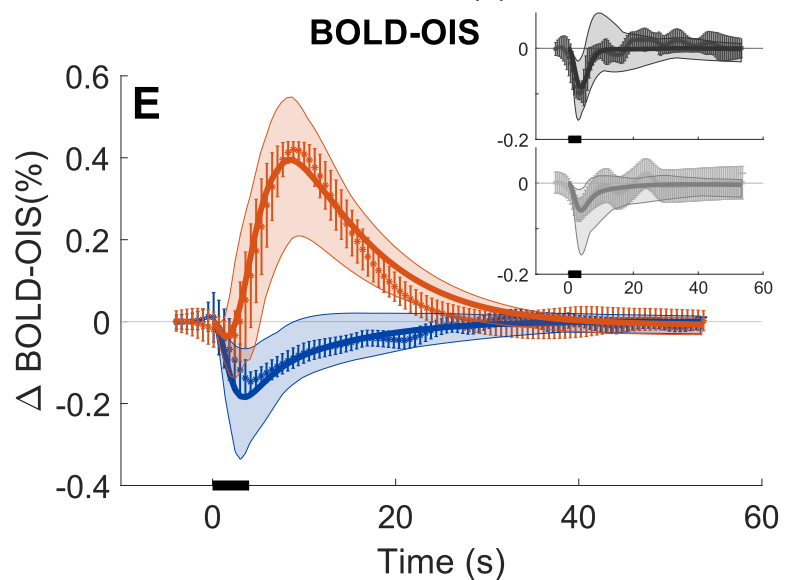
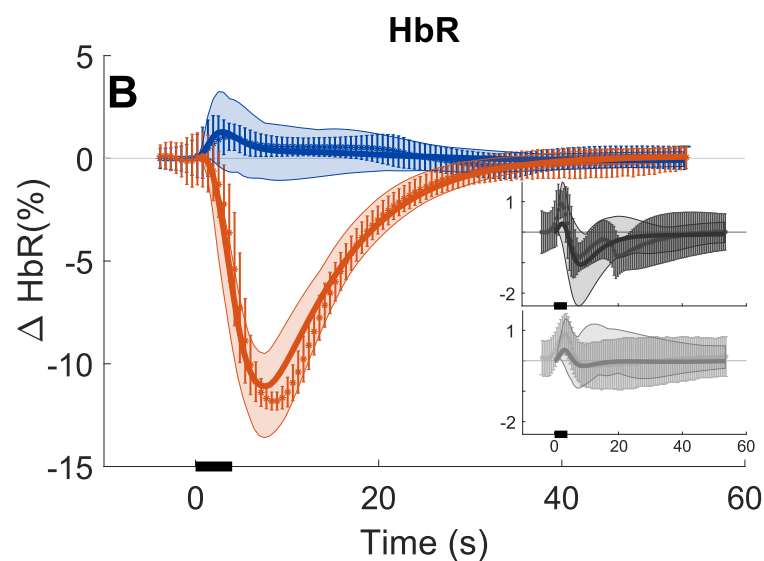
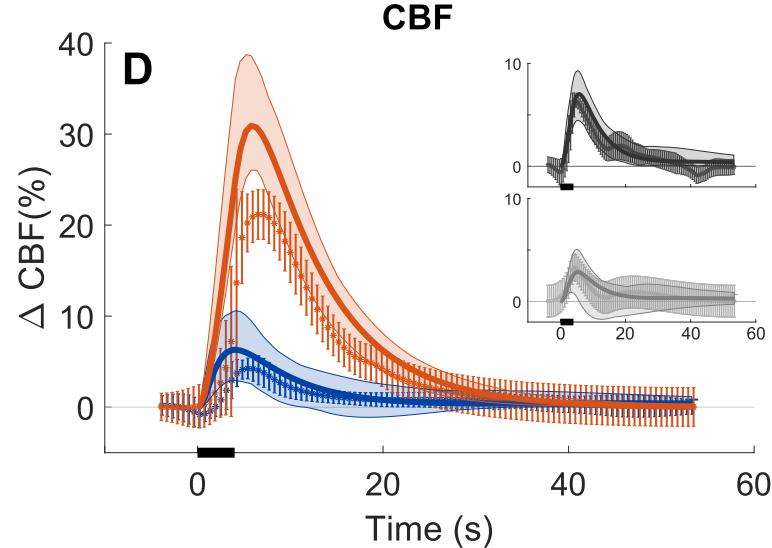
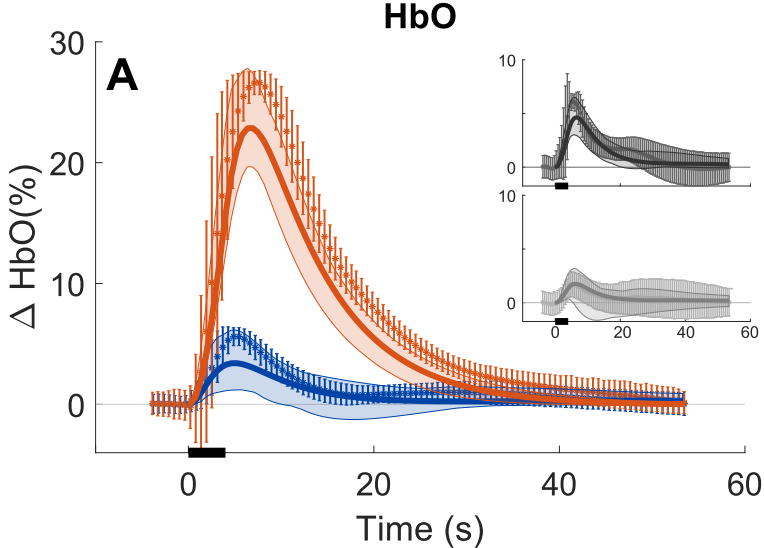


C Relative Contribution to CMRO₂



D





✦ Experimental data — Model Simulation

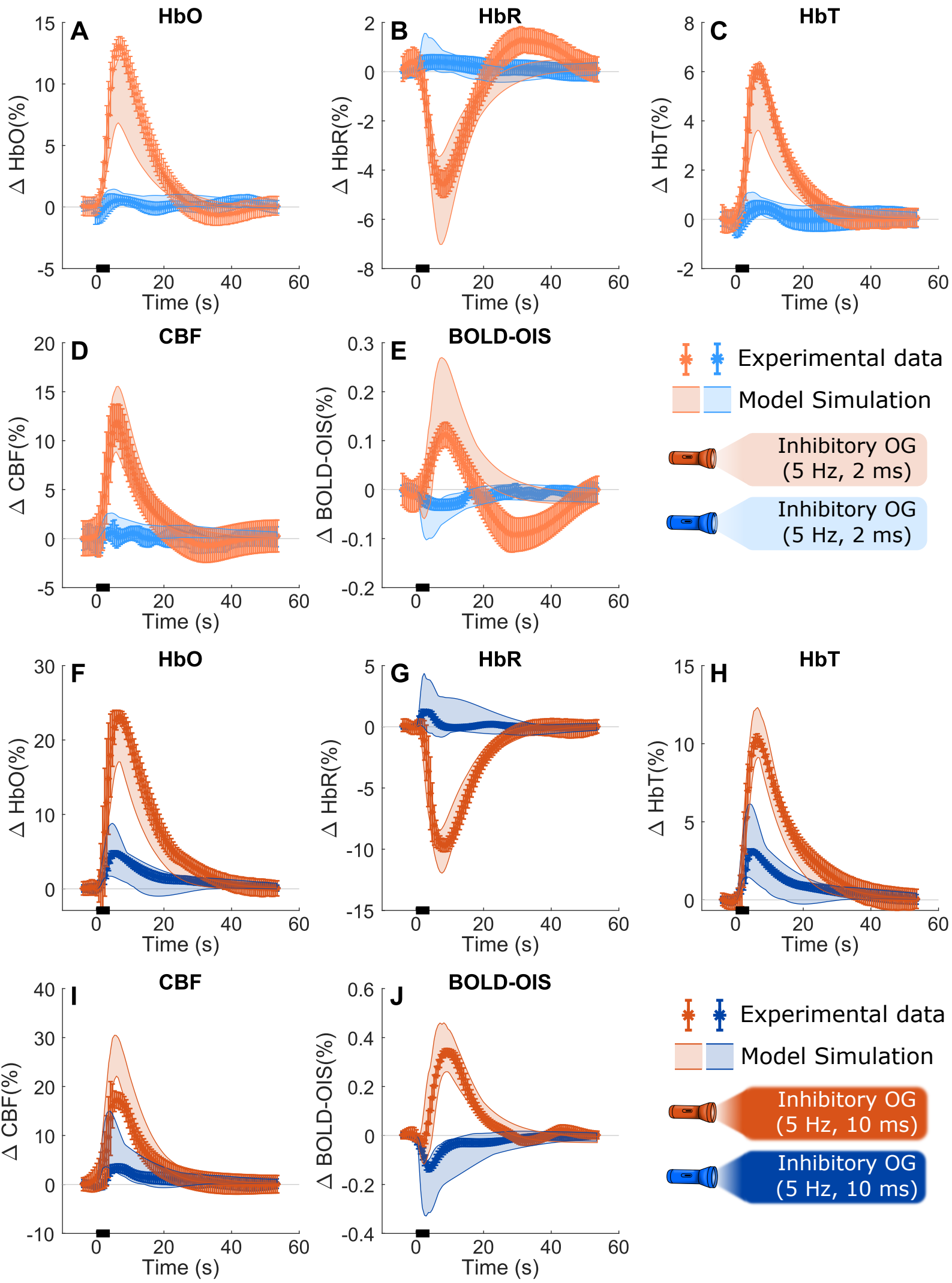
🔊 Inhibitory OG stimulation (5 Hz)

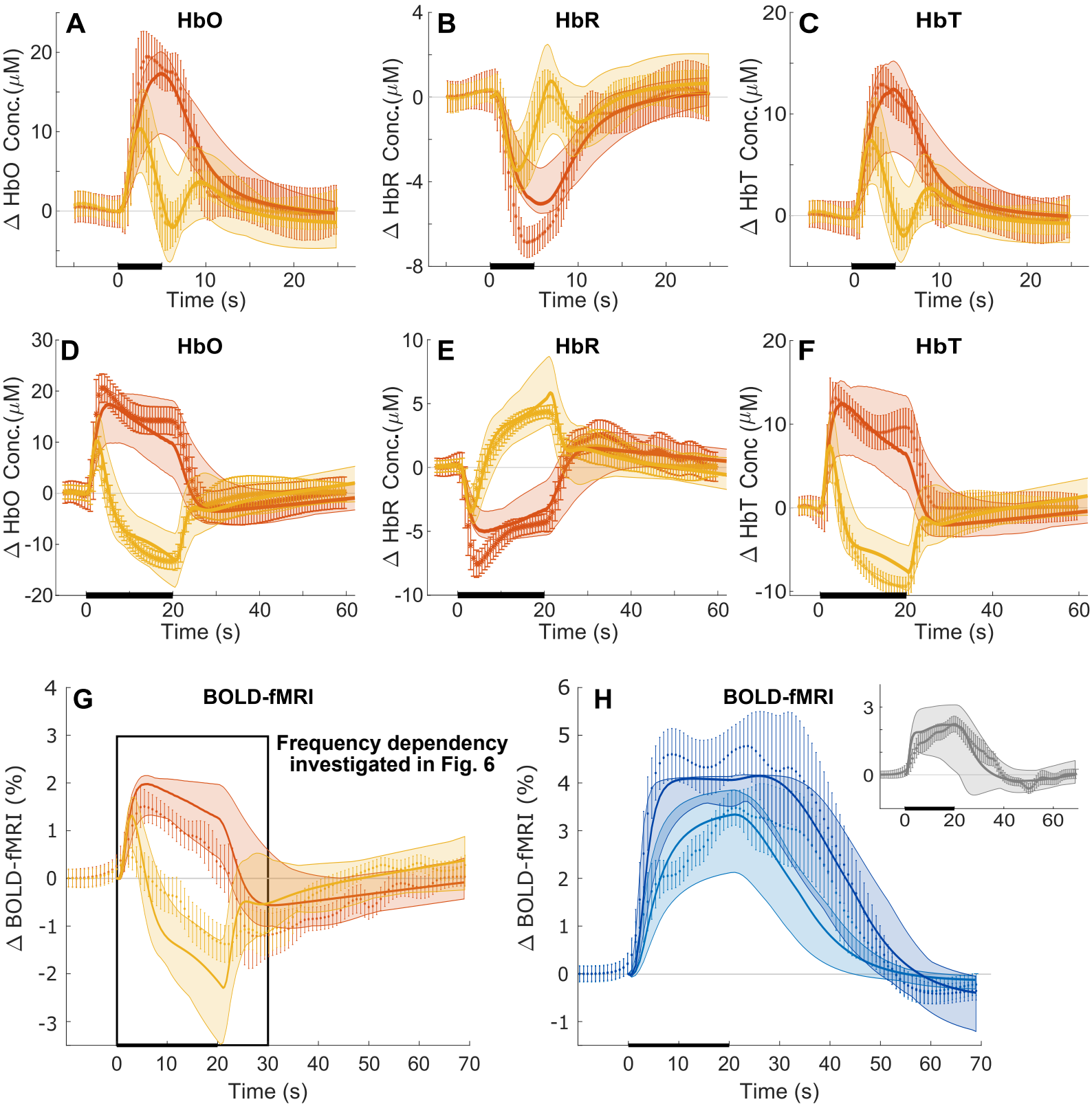
🔊 Excitatory OG stimulation (5 Hz)

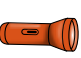
⚡ Sensory stimulation (Excitatory-line)


⚡ Sensory stimulation (Inhibitory-line)


Model Predictions









 Inhibitory Stimulation
 Low Intensity (1 Hz)

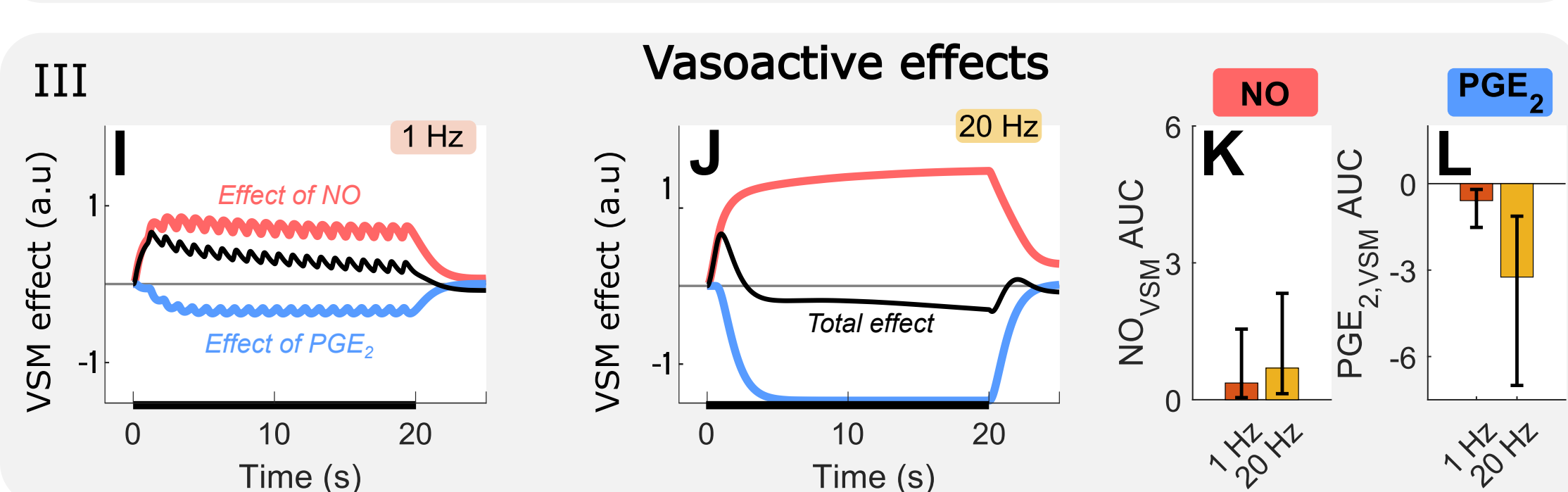
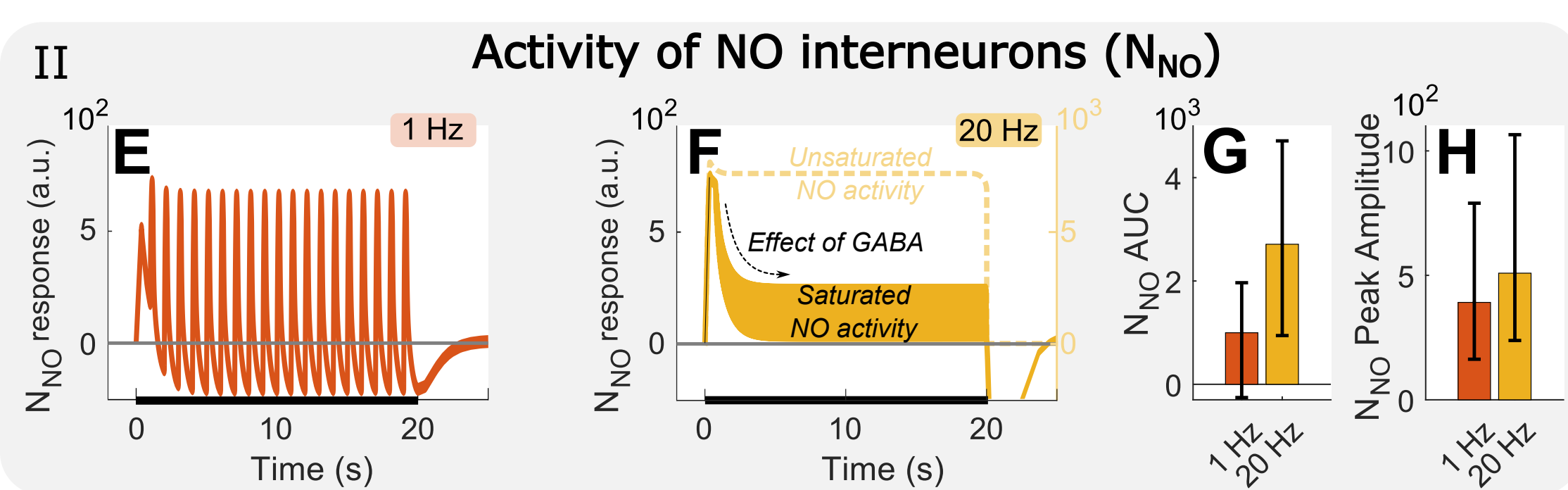
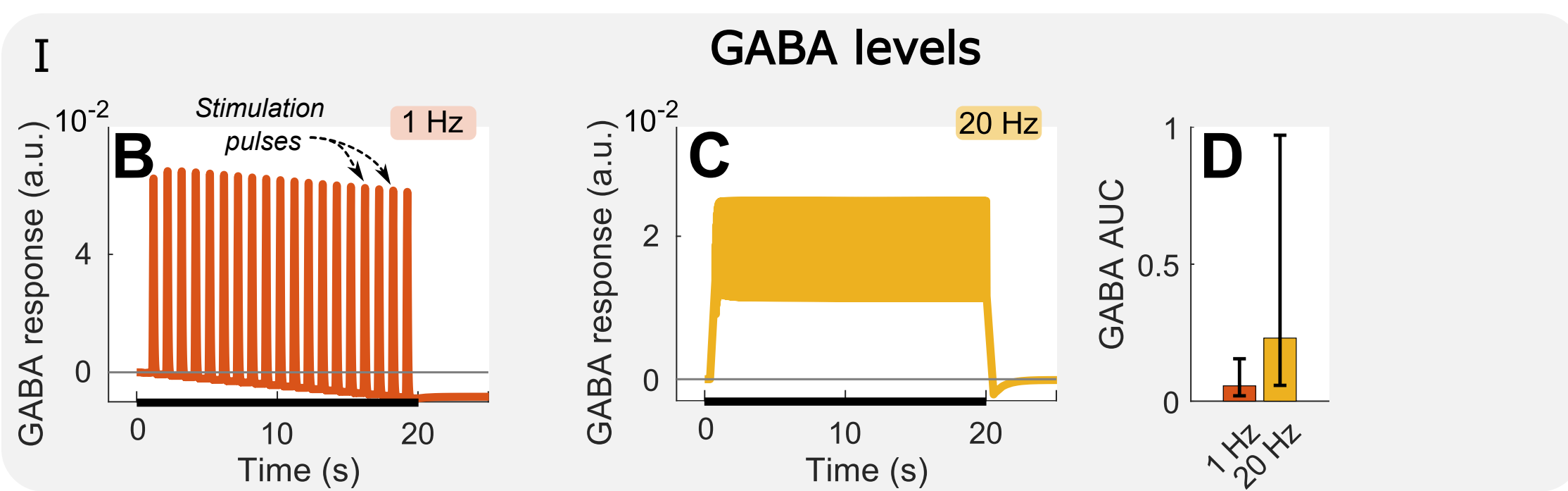
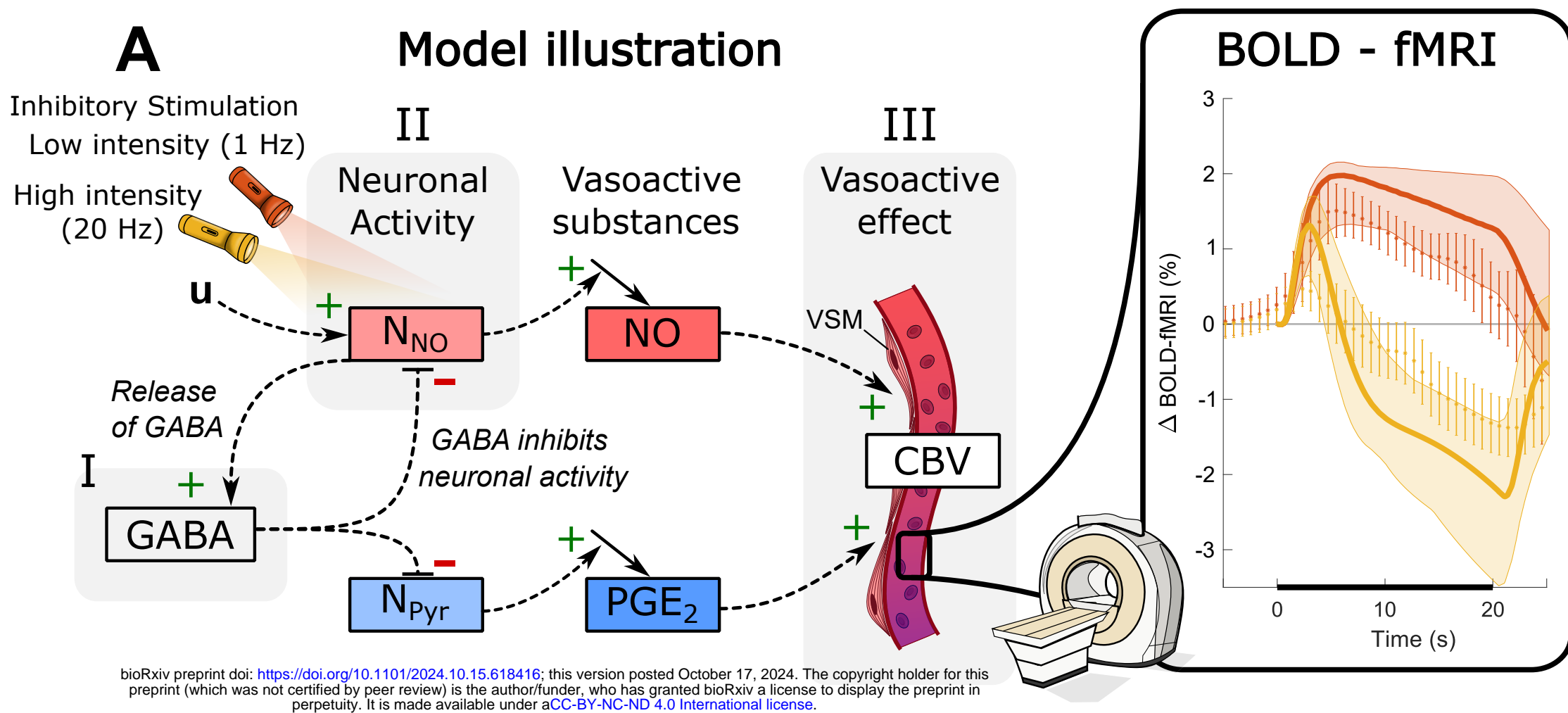
 Excitatory Stimulation
 Low Intensity (1 Hz)

 Sensory
 Stimulation (4 Hz)

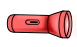
 Inhibitory Stimulation
 High Intensity (20 Hz)


 Excitatory Stimulation
 High Intensity (20 Hz)

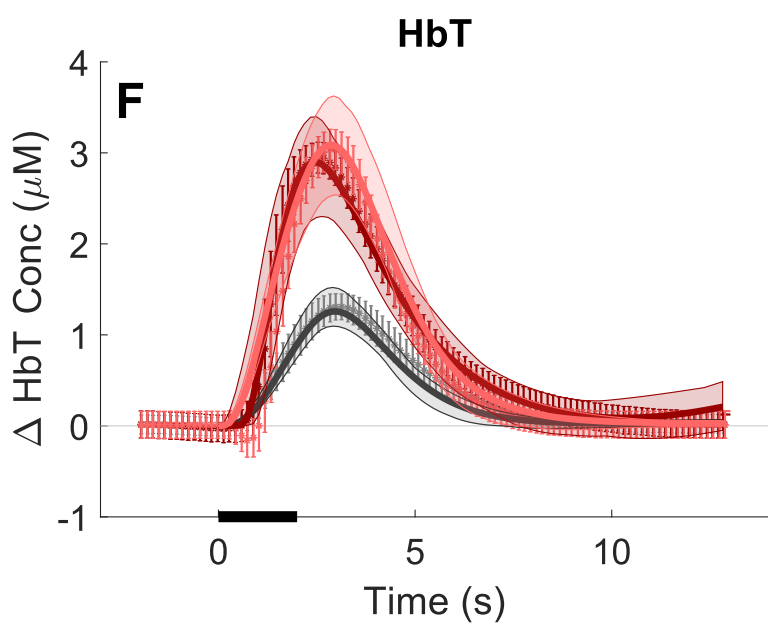
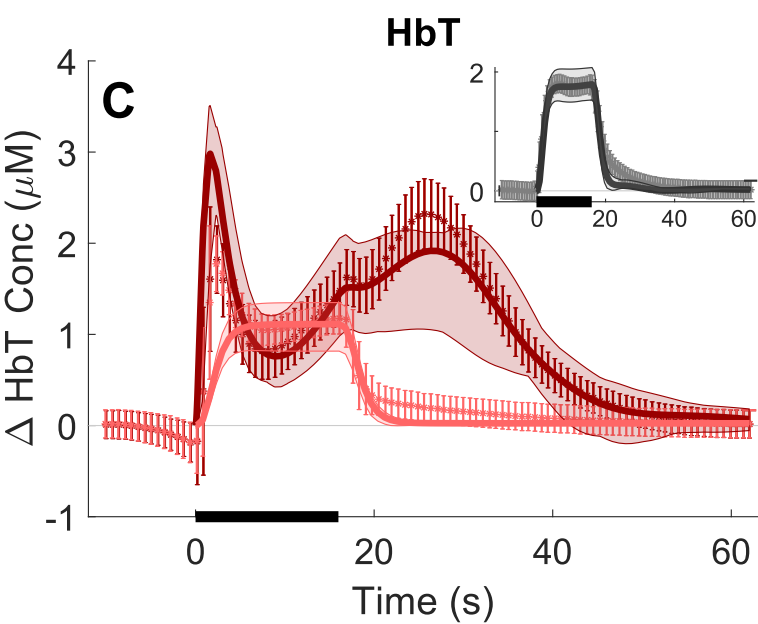
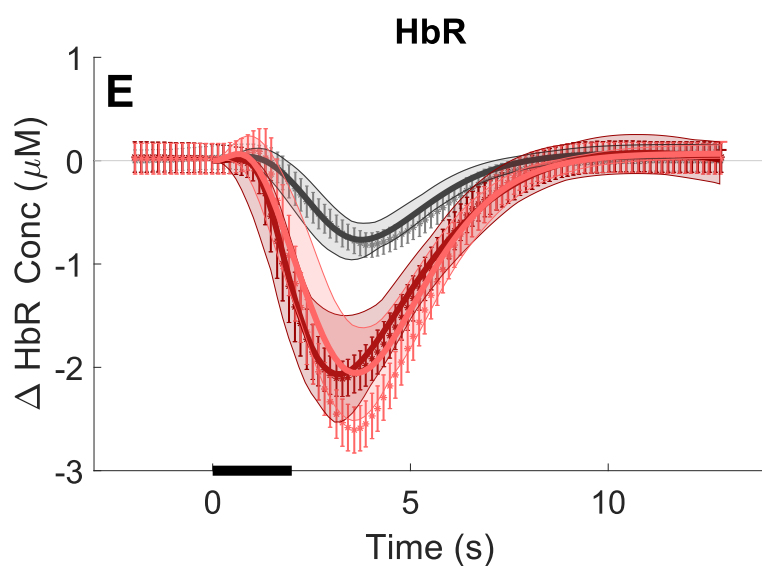
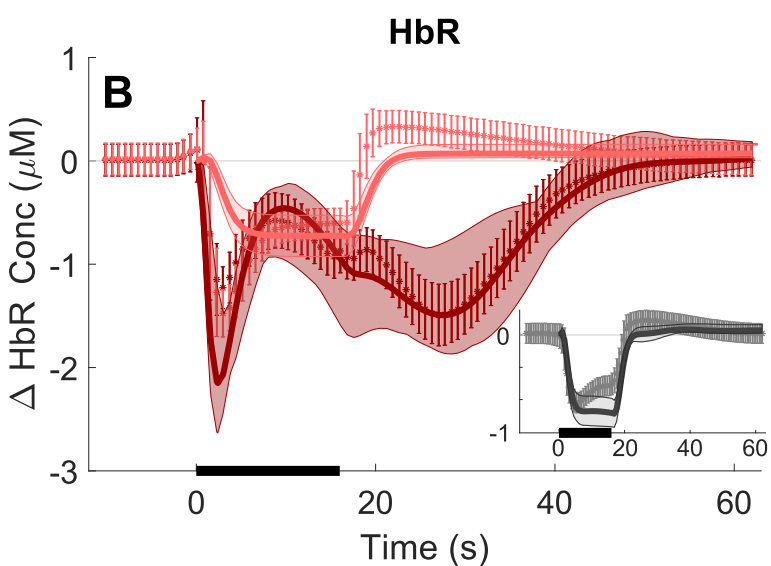
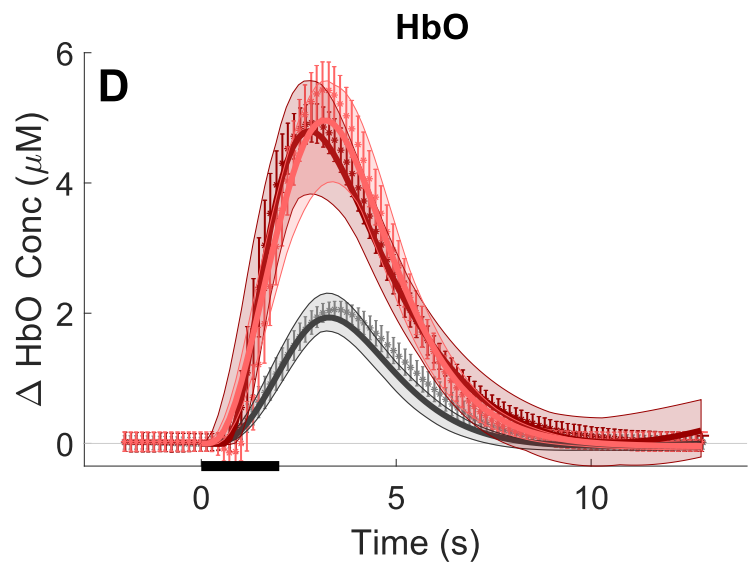
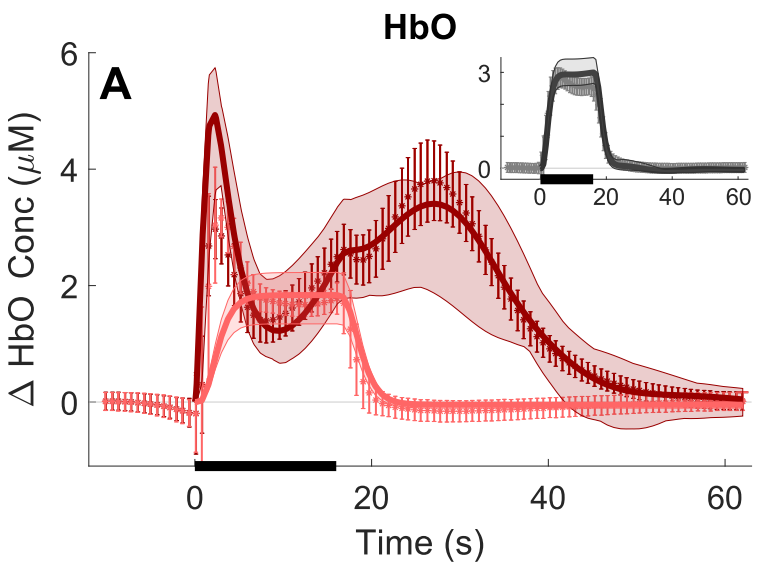
 Experimental data
 Model Simulation



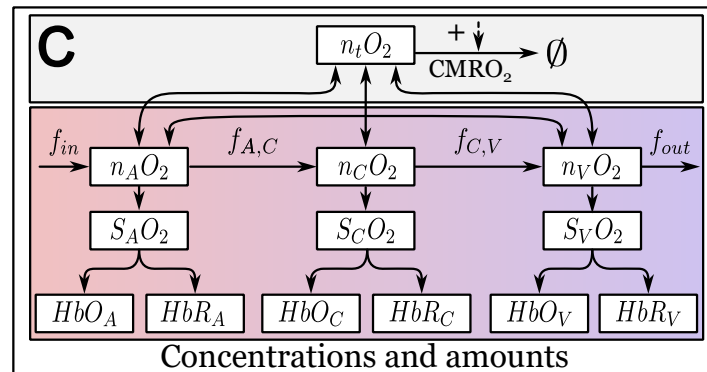
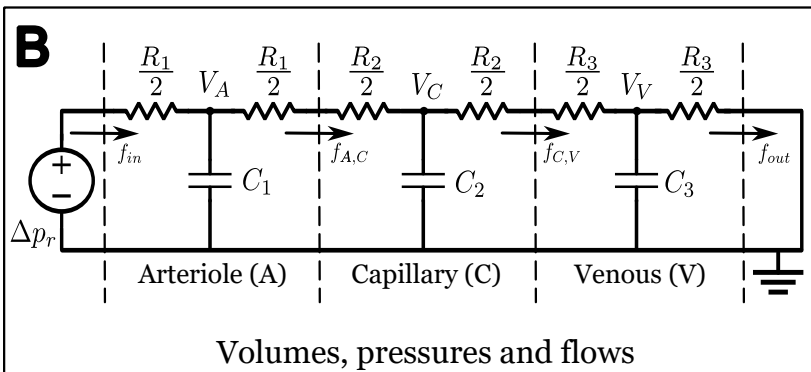
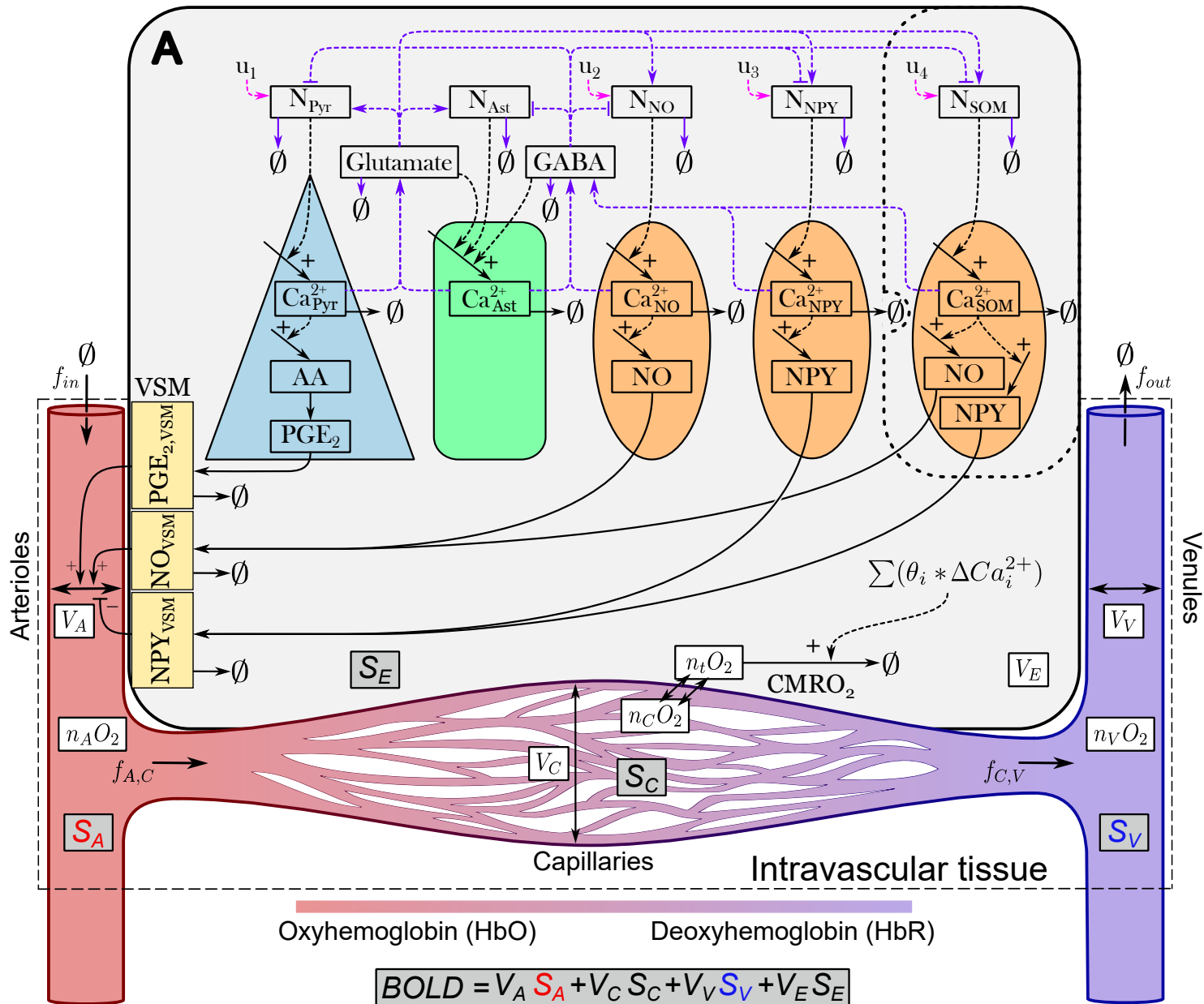
 SST (SOM) 20 Hz

 nNOS (NO) 20 Hz

 Whiskers 5 Hz



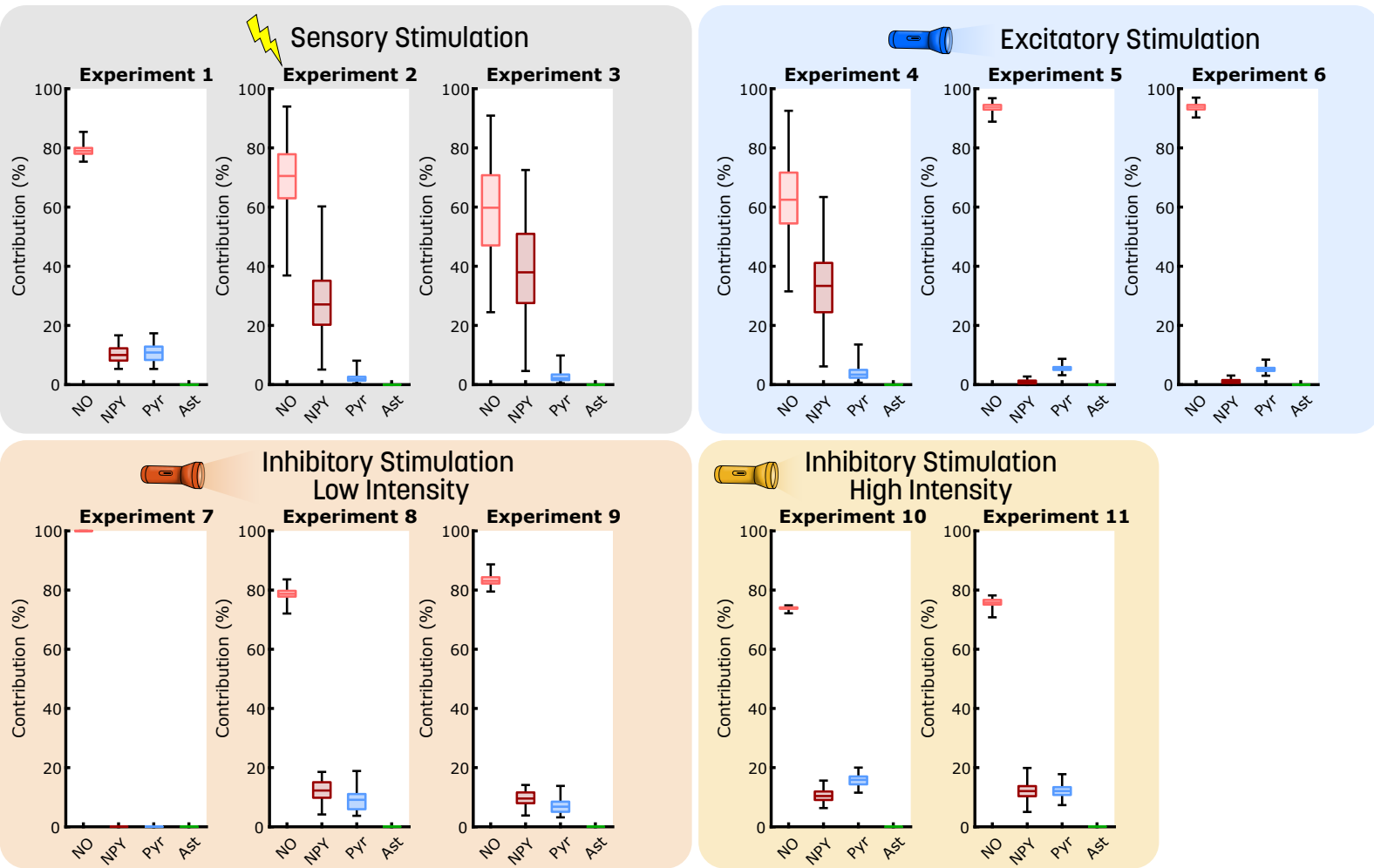
Extravascular tissue



A

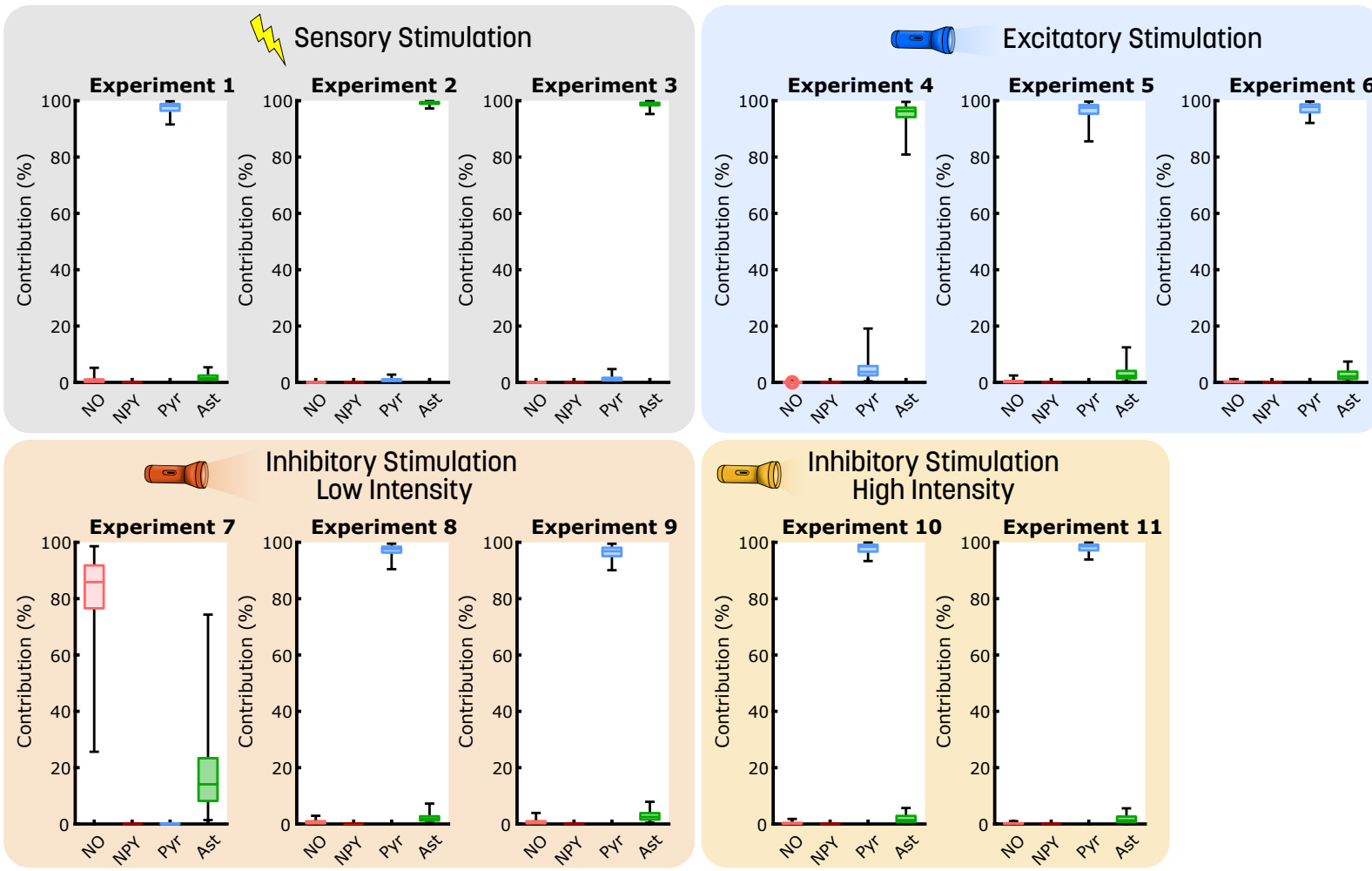
Relative Contribution to CBV Signal

■ NO Interneurons
 ■ NPY Interneurons
 ■ Pyramidal Neurons
 ■ Astrocytes



B

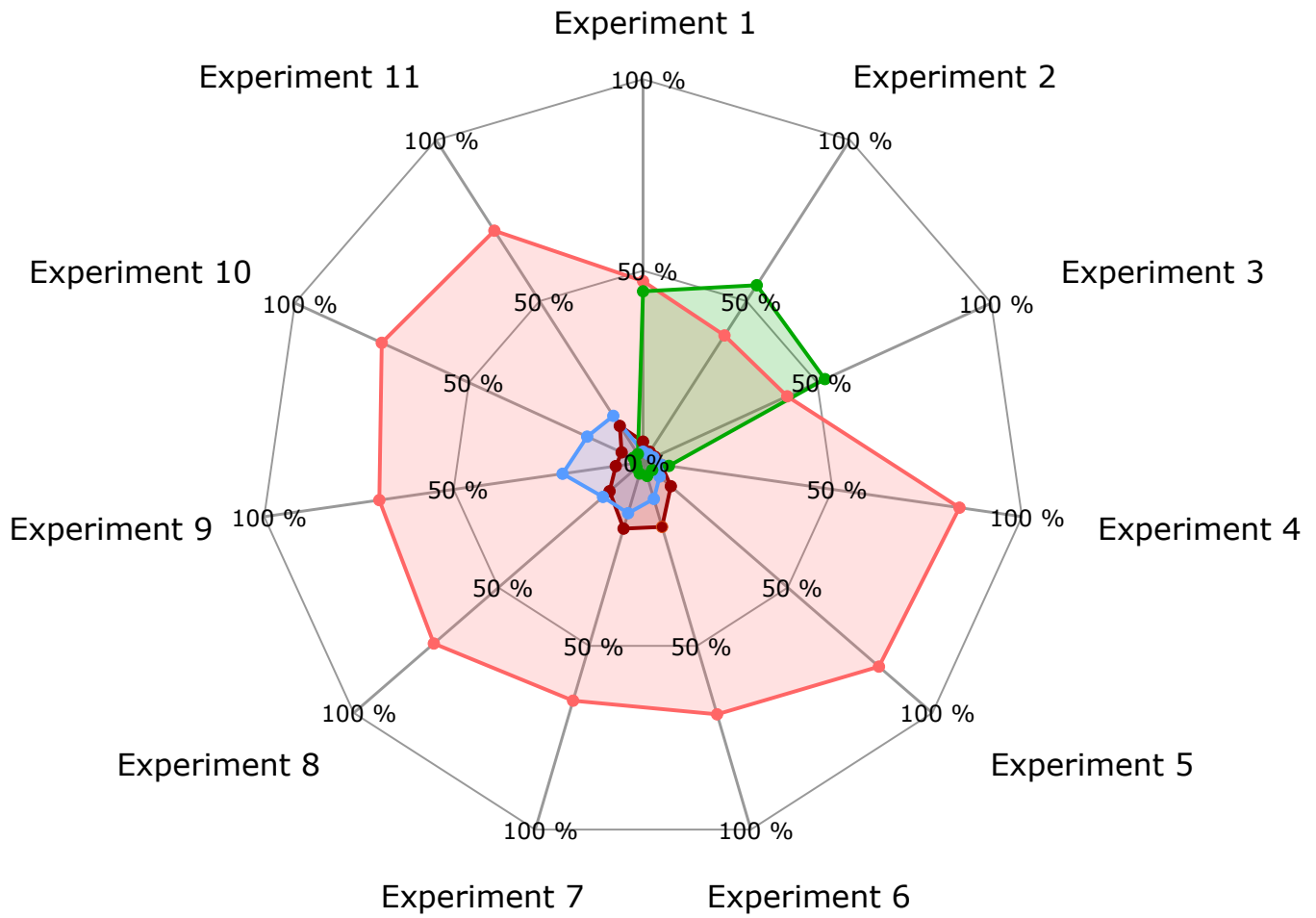
Relative Contribution to CMRO₂ Signal



A

Relative Contribution to HoR Signal

NO Interneurons Pyramidal Neurons
 NPY Interneurons Astrocytes



B

